

# Full spectrum fitting with photometry in ppxf: non-parametric star formation history, metallicity and the quenching boundary from 3200 LEGA-C galaxies at redshift $z \approx 0.8$

Michele Cappellari<sup>★</sup>

*Sub-Department of Astrophysics, Department of Physics, University of Oxford, Denys Wilkinson Building, Keble Road, Oxford, OX1 3RH, UK*

Submitted to MNRAS on 31 August 2022

## ABSTRACT

I start by describing some updates to the ppxf method, which has been used to measure stellar and gas kinematics as well as the formation history (SFH) and chemical composition of galaxies. I outline the novel linearly-constrained least-squares optimization algorithm used by ppxf and I illustrate the changes I made to be able to include photometric measurements together with full-spectrum fitting in ppxf. Then I present an application of the revised ppxf method to the study of the non-parametric SFH and metallicity  $[M/H]$  of a sample of 3200 galaxies at redshift  $0.6 < z < 1$  (median  $z = 0.76$ ), complete above a stellar mass  $M_* \gtrsim 3 \times 10^{10} M_\odot$ , with spectroscopy from the LEGA-C survey and 28-bands photometry from two alternative catalogues. I extract and compare the stellar population using three independent stellar population synthesis (SPS) methods and both photometric catalogues. I find robust trends in the global light-weighted ages and  $[M/H]$  consistent and of similar quality as those from nearby galaxy surveys, with the well-known main dependence on the galaxies' stellar velocity dispersion  $\sigma_*$  (or alternative measures of central density). The recovered SFH indicate a sharp and strikingly clear boundary from star formation to quenching at  $\lg(\sigma_*/\text{km s}^{-1}) \approx 2.3$ , similar to what is invoked by some models. Equally clear quenching boundaries are seen at  $[M/H] \approx -0.1$  and for a Sersic index  $\lg n_{\text{Sers}} \approx 0.5$ . Results are consistent with two SPS methods and both photometric catalogues, but the third SPS method displays significant differences, highlighting the importance of comparing model assumptions. The ppxf software is available from <https://pypi.org/project/ppxf/>.

**Key words:** galaxies: evolution – galaxies: formation – galaxies: high-redshift – software: data analysis – techniques: photometric – techniques: spectroscopic

## 1 INTRODUCTION

The study of the stellar population of galaxies is an essential tool when trying to uncover how they have assembled. For this reason, a vast number of papers have tried to infer the galaxies' star formation history (SFH) and chemical composition from observations. The earliest results were based on simple galaxy colours as these were easier to obtain (see e.g. the lectures by Baade 1963). However, galaxy colours alone cannot strongly constrain both the galaxies' chemical composition and star formation histories. Inferences from galaxy photometry alone are strongly affected for example by the age-metallicity (e.g. Worthey 1994) as well as by the SFH-dust degeneracies (e.g. Silva et al. 1998; Devriendt et al. 1999; Pozzetti & Mannucci 2000). For this reason, most of our knowledge on both the star formation and chemical composition of galaxies has been obtained from the numerous absorption features in their spectra.

### 1.1 Full spectrum fitting of nearby galaxies

Over the past two decades, libraries of high-resolution ( $R \gtrsim 2000$ ) empirical stellar spectra were observed, which try to optimally sam-

ple all stages of stellar evolution. Prominent examples in the optical region include the STELIB (Le Borgne et al. 2003), ELODIE (Prugniel & Soubiran 2001), MILES (Sánchez-Blázquez et al. 2006; Falcón-Barroso et al. 2011) and recently the MaStar (Yan et al. 2019) stellar libraries. An exception is the X-Shooter spectral library (XSL), which reaches  $R \approx 10000$  and extends up to  $2.5 \mu\text{m}$  (Chen et al. 2014; Verro et al. 2022a).

Stellar population synthesis SPS models based on empirical stellar spectra have been developed that can produce synthetic galaxy spectra at high resolution. Examples of these kind of models are the GALAXEV (Bruzual & Charlot 2003), the Vazdekis (Vazdekis et al. 2010, 2015), the fSPS (Conroy et al. 2009; Conroy & Gunn 2010), the Maraston (Maraston 2005; Maraston & Strömbäck 2011; Maraston et al. 2020) and most recently the XSL models (Verro et al. 2022b). Most current SPS models complement empirical stellar spectra with fully synthetic ones like BaSel (Westera et al. 2002) or MARCS (Gustafsson et al. 2008). This allows one to cover stages of stellar evolution not well sampled by observations and also can extend the wavelength coverage, especially to the ultraviolet and infrared regions which are poorly covered by observations. Fully synthetic SPS were also developed like BPASS (Stanway & Eldridge 2018; Byrne et al. 2022) or the MARCS version of the Maraston models.

Initially, large spectroscopic studies of the stellar population in

<sup>★</sup> E-mail: michele.cappellari@physics.ox.ac.uk

nearby galaxies were based on line indices of specific absorption features, generally using the LICK system (e.g. [Worley et al. 1994](#)). But the availability of good-quality high-resolution SPS models (see review by [Conroy 2013](#)) motivated a shift to using full-spectrum fitting (see review by [Walcher et al. 2011](#)). Various templates-fitting methods were developed for this task, like PPXF ([Cappellari & Emsellem 2004; Cappellari 2017](#)), STARLIGHT ([Cid Fernandes et al. 2005](#)), STECMAP ([Ocvirk et al. 2006](#)), VESPA ([Tojeiro et al. 2007](#)), fIT3D ([Sánchez et al. 2016; Lacerda et al. 2022](#)) and FIREFLY ([Wilkinson et al. 2017](#)). These methods and software were extensively used e.g. to analyse the millions of spectra produced by integral-field spectroscopic surveys in the local Universe like ATLAS<sup>3D</sup> ([Cappellari et al. 2011](#)), CALIFA ([Sánchez et al. 2012](#)), SAMI ([Bryant et al. 2015](#)) and MaNGA ([Bundy et al. 2015](#)).

## 1.2 Spectral fitting of high- $z$ galaxies

At significant redshift (e.g.  $z \gtrsim 1$ ) the cosmological surface brightness dimming (e.g. [Hogg 1999](#)) makes good-quality spectra more difficult to obtain as the contribution of the sky background starts to dominate. PPXF was used to measure the kinematic and stellar population of significant samples of galaxies at redshift  $z \approx 1$  (e.g. [Shetty & Cappellari 2015; Bezanson et al. 2018](#)) but only of individual objects out to  $z \approx 2$  (e.g. [van de Sande et al. 2013; Belli et al. 2014, 2017](#)) and  $z \approx 3$  (e.g. [Esdale et al. 2021; Forrest et al. 2022](#)). Most large studies of distant galaxies still had to rely on photometry alone.

The most essential parameters one wants to extract from high- $z$  galaxies are their redshift and stellar mass (e.g. [Muzzin et al. 2013; Weaver et al. 2022](#)). Various template-fitting codes were developed to measure masses and redshift from photometric observations in multiple bands (I ignore here methods based on machine learning; see [Salvato et al. 2019](#) for a review). These include HYPERZ ([Bolzonella et al. 2000](#)), BPZ ([Benítez 2000](#)), LePHARE ([Arnouts et al. 2002](#)), ZEBRA ([Feldmann et al. 2006](#)) and EAZY ([Brammer et al. 2008](#)). These methods are conceptually similar to the template-based spectral fitting ones used for nearby galaxies, however, they all adopt a Bayesian approach, instead of a least-square fitting one. This makes the codes simpler and allows for easy inclusion of priors on galaxy parameters or non-Gaussian uncertainties; e.g. one can assign a low probability to solutions where the galaxy has an unphysically large/small stellar mass.

Some of the photometric-redshift methods were subsequently extended and new software were developed to fit spectra together with the photometry, while still retaining the same Bayesian approach. Examples of these are FAST ([Kriek et al. 2009](#)), BEAGLE ([Chevallard & Charlot 2016](#)), BAGPIPES ([Carnall et al. 2018](#)), the code described by [Mendel et al. \(2020\)](#) and PROSPECTOR ([Johnson et al. 2021b](#)).

Contrary to what is sometimes stated, *both* least-squares, or maximum-likelihood, and Bayesian methods can return model posteriors, when needed. The former uses bootstrapping (e.g. [Efron & Tibshirani 1994](#)) or Monte Carlo approaches. In fact, bootstrapping can be seen as an efficient way to compute the Bayesian posterior, with non-informative priors (e.g. [Rubin 1981; Efron 2011](#)). Although bootstrapping is less flexible than general Bayesian methods, in many realistic situations, the uncertainties of model parameters are dominated by data systematic and model assumptions (as I also find later) rather than the details of the adopted statistical approach or by adopted priors.

## 1.3 This paper

In this paper, I proceed in a different way than existing methods. Instead of adopting the standard Bayesian approach to fit photometry and spectra, I present an extension of a least-squares full-spectrum fitting method to simultaneously fit photometry. I do this using my PPXF code. A key difference of this approach is that it can be a few orders of magnitude faster than Bayesian methods. The method appears complementary to existing ones as the extra speed allows for extra flexibility in the treatment of the stellar population, as shown later.

I illustrate the characteristics of the approach by fitting the VIMOS spectra and COSMOS photometry ([Muzzin et al. 2013; Weaver et al. 2022](#)) to study the joint SFH - metallicity distributions and the stellar population scaling relations of about 3200 galaxies from the LEGA-C survey ([van der Wel et al. 2021](#)) in the redshift range  $z = 0.6 - 1$ .

Readers interested in the PPXF techniques should keep reading how to measure velocities in [Section 2](#) and the PPXF updates in [Section 3](#). While those only interested in the scientific results should skip the next two sections and go directly to the description of the data in [Section 4](#) and results in [Section 6](#). In this work I adopt a standard cosmology with  $H_0 = 70 \text{ km s}^{-1}\text{Mpc}^{-1}$ ,  $\Omega_m = 0.3$  and  $\Omega_\Lambda = 0.7$ .

## 2 MEASURING VELOCITY AND REDSHIFT

In [Cappellari \(2017, sec. 2\)](#) I reviewed general and important facts that one should know before using any full spectral fitting method and PPXF in particular. Here I include only some updates, and I heavily refer the reader to my previous paper of this series to avoid duplicating material.

### 2.1 From measured velocity to observed redshift

The physical meaning of the velocity  $V$  returned by PPXF or any spectrum fitting code is often a source of confusion. As discussed in [Cappellari \(2017, sec. 2.3\)](#), the reason for this is that  $V$  has no physical meaning. Even the recession velocity itself, for a distant galaxy, is an ill-defined concept with a debated interpretation (e.g. [Bunn & Hogg 2009](#)). It should never be used for quantitative work. What is well defined empirically is the redshift  $z$  of a given spectrum:

$$1 + z \equiv \frac{\lambda_{\text{obs}}}{\lambda_{\text{emit}}}, \quad (1)$$

where  $\lambda_{\text{obs}}$  and  $\lambda_{\text{emit}}$  are the observed and rest-frame wavelength of a given spectral feature. The key formula that is needed to convert the  $V_{\text{PPXF}}$  returned by PPXF into redshift is eq. (8) of [Cappellari \(2017\)](#)

$$V_{\text{PPXF}} \equiv c \ln(1 + z), \quad (2)$$

with  $c$  the speed of light. This formula is exact by construction and it is the only one that should be used to attach a physical meaning to  $V_{\text{PPXF}}$ .

### 2.2 Separating peculiar velocities and cosmological redshift

When observing spectra of distant galaxies from a single aperture, redshift is all one can measure. However, when obtaining spatially-resolved observations of galaxies e.g. using integral-field spectroscopy (see review by [Cappellari 2016](#)) one needs to separate the cosmological redshift  $z_{\text{cosm}}$ , which only contains information on

the galaxy distance, from the peculiar velocity  $V_{\text{pec}}$ . The latter is the one which satisfies e.g. Newton's law of gravitation in a reference system that moves with the galaxy barycentre. It is the velocity that has to be used to construct dynamical models of the galaxy.

In Cappellari (2017, sec. 2.4) I suggested using the standard way of separating peculiar and cosmological redshift. However, there is a simpler and formally even more accurate way. In fact, the conversion of  $V_{\text{ppxf}}$  into redshift is unnecessary (see Baldry 2018). One can directly obtain  $V_{\text{pec}}$  using the velocities returned by PPXF as follows

$$V_{\text{pec}}(x, y) = V_{\text{ppxf}}(x, y) - V_{\text{ppxf}}(\text{bary}). \quad (3)$$

Here  $V_{\text{ppxf}}(x, y)$  is the velocity returned by PPXF at the location  $(x, y)$  on the sky,  $V_{\text{ppxf}}(\text{bary})$  is the velocity returned by PPXF for the galaxy (or cluster) barycentre and  $V_{\text{pec}}(x, y)$  is the peculiar velocity at location  $(x, y)$ . The latter is the only one with a clear physical meaning: it is the one to use in a dynamical model (e.g. Cappellari 2008), or to estimate the level of rotation in a galaxy (e.g. Emsellem et al. 2011). Importantly, equation (3) is always valid, regardless of whether the spectrum was de-redshifted to the rest-frame or not, before measuring  $V_{\text{ppxf}}$ . Note that this formula only works because of the way PPXF defines the relation between velocity and redshift in equation (2) and *cannot* be used with alternative definitions (e.g.  $V \equiv cz$ ).

As an example of a practical application of these formulas, let's assume I am fitting a single spectrum of a high- $z$  galaxy for which I have an estimate of the redshift  $z'$  (e.g. from photometry). It is generally convenient to de-redshift the spectrum by dividing each observed wavelength  $\lambda_{\text{obs}}$  to obtain an estimate of the rest-frame wavelength with

$$\lambda'_{\text{rest}} = \frac{\lambda_{\text{obs}}}{(1 + z')} \quad (4)$$

I then fit the spectrum with PPXF to obtain  $V_{\text{ppxf}}$ . If the initial guess  $z'$  was perfect, I would obtain  $V_{\text{ppxf}} = 0$ , but in general I will measure  $V_{\text{ppxf}} \neq 0$ , with uncertainty  $\Delta V_{\text{ppxf}}$ . An improved estimate of the galaxy redshift  $z$  and its uncertainty  $\Delta z$  can be obtained using equation (2) and equation (3) as

$$V' = c \ln(1 + z'), \quad (5a)$$

$$V_{\text{tot}} = V_{\text{ppxf}} + V' \quad (5b)$$

$$1 + z = \exp\left(\frac{V_{\text{tot}}}{c}\right) = (1 + z') \exp\left(\frac{V_{\text{ppxf}}}{c}\right) \quad (5c)$$

$$\frac{\Delta z}{1 + z} \approx \Delta \ln(1 + z) \approx \frac{\Delta V_{\text{ppxf}}}{c}. \quad (5d)$$

Identical results are obtained without first bringing the spectrum to the restframe and setting  $z' = 0$  in equation (5). But one should remember to adjust the instrumental resolution as described in sec. 2.4 of Cappellari (2017).

### 3 UPDATES TO THE PPXF PACKAGE

I gave a detailed overview of the PPXF method in Cappellari (2017, sec. 3). I will not repeat that overview here, but instead, I will refer the reader to specific sections of that paper, while trying to keep a consistent notation. However, I substantially evolved PPXF since then, driven by the needs of my research and requests from colleagues. I only describe here the PPXF features that have changed. The description corresponds to the current version 8.2 of the public PPXF Python package<sup>1</sup>.

<sup>1</sup> Available from <https://pypi.org/project/ppxf/>

### 3.1 Well-sampled variable- $\sigma$ convolution

As discussed in Cappellari (2017, sec. 2.2), when fitting stellar templates to galaxy spectra, one generally needs to convolve the templates with a Gaussian having a dispersion  $\sigma$  that varies with wavelength  $\lambda$ . In a previous version of PPXF, I implemented this step as a direct summation of the spectrum, weighted by the Gaussian centred on every pixel (function `ppxf.util.gaussian_filter1d` in PPXF). Given that the Gaussian is typical nonzero only over  $n_{\text{gau}} \sim 10$  pixels, while the templates have  $n_{\text{pix}} \sim 1000$  spectral pixels, I limited the summation only to the nonzero pixels of the Gaussian kernel. In this way, the computation time of this summation scales as  $t \propto n_{\text{pix}} \times n_{\text{gau}}$ , which is comparable to that  $t \propto n_{\text{pix}} \times \ln(n_{\text{pix}})$  achievable using Fourier convolution using the Fast Fourier Transform (FFT, Cooley & Tukey 1965).

A limitation of performing a convolution as a summation is that, when the  $\sigma$  of the Gaussian becomes comparable to the size of the sampled pixels, the convolution suffers from the same undersampling problems that motivated the use of an analytic Fourier Transform for the convolution in PPXF discussed in Cappellari (2017). For this reason, I now implemented an alternative procedure `ppxf.util.varsmooth` which performs the variable- $\sigma$  convolution using the FFT and uses the same approach of PPXF of using an analytic Fourier Transform of the kernel, to avoid undersampling issues.

A natural idea to use the FFT for convolution of a vector of values with a kernel with variable scale is to stretch the coordinate with the inverse of the scale, via interpolation, in such a way that the kernel has the same scale in the new coordinates. This idea was discussed e.g. in 2014 on StackOverflow<sup>2</sup> and implemented in 2016 by Janez Kos on GitHub<sup>3</sup> in the procedure `varconvolve`. It was also discussed in Johnson et al. (2021b). The interpolation approach is also central for algorithms for the Non-Uniform FFT (NUFFT, e.g. Greengard & Lee 2004). Here I combine the interpolation approach with the use of an analytic Fourier Transform as in Cappellari (2017) to produce Algorithm 1. The algorithm can also be used with a non-Gaussian kernel (e.g. Cappellari 2017, eq. 38) as long as only its scale changes with wavelength.

#### Algorithm 1 `varsmooth`: well-sampled variable- $\sigma$ convolution

---

Given $\mathbf{x}, \mathbf{y}, \sigma_x, \mathbf{x}_{\text{out}}$	$\triangleright \text{len}(\mathbf{x}) = \text{len}(\mathbf{y}) = \text{len}(\sigma_x) = p$
$\sigma = \sigma_x / \nabla \mathbf{x}$	$\triangleright \sigma$ in pixels
$\sigma_{\text{max}} = \max(\sigma) \times m$	$\triangleright$ Optional $m$ = oversampling
<b>for</b> $k = 1, p$ <b>do</b>	
$s_k = \sum_{j=1}^k (\sigma_{\text{max}} / \sigma_j)$	$\triangleright \sigma$ is constant in $\mathbf{s}$ coordinates
$n = \text{ceil}(s_p - s_1)$	$\triangleright$ Ensures $\sigma > m$ in new pixels
$\mathbf{x}_{\text{new}} = \text{subdivide}(s_1, s_p, n)$	$\triangleright n$ equispaced values
$\mathbf{y}_{\text{new}} = \text{interpolate}(\mathbf{s}, \mathbf{y})(\mathbf{x}_{\text{new}})$	
$\mathcal{F}(\text{gauss}) = \exp(-\sigma_{\text{max}}^2 \omega^2 / 2) / \sqrt{2\pi}$	$\triangleright$ Gaussian Analytic FT
$\mathbf{y}_{\text{conv}} = \mathcal{F}^{-1}[\mathcal{F}(\mathbf{y}_{\text{new}})\mathcal{F}(\text{gauss})]$	$\triangleright$ Convolution theorem & FFT
<b>if</b> $\mathbf{x}_{\text{out}}$ is given <b>then</b>	
$\mathbf{s} = \text{interpolate}(\mathbf{x}, \mathbf{s})(\mathbf{x}_{\text{out}})$	
$\mathbf{y}_{\text{conv}} = \text{interpolate}(\mathbf{x}_{\text{new}}, \mathbf{y}_{\text{conv}})(\mathbf{s})$	

---

This algorithm works well in practice, but one should be aware of its theoretical limitations. In fact, most interpolation methods can be described as a convolution with a specific kernel (e.g. Getreuer 2011) and one may think it would be better to remove the effect of this extra convolution as done e.g. in the NUFFT methods. However, this

<sup>2</sup> <https://stackoverflow.com/a/24186800>

<sup>3</sup> <https://github.com/sheliak/varconvolve>

situation is different as the spectra have noise and one would have to perform the interpolation in a Bayesian framework (e.g. MacKay 1992, 2003). One should also consider that the spectra to fit generally already include additional interpolation and resampling, which would have to be modelled for rigorous results. But all this is unlikely to affect scientific results, and for this reason, is beyond the scope of this paper.

### 3.2 CAPFIT nonlinear least-squares with linear constraints

#### 3.2.1 The problem

When fitting the kinematics of multiple kinematics components with PPXF, both for the stellar and gas emission components, it is often useful to be able to set constraints on some parameters as a function of other parameters. For example, when looking for spectra containing both narrow and broad gas emission lines to study Active Galactic Nuclei (e.g. Oh et al. 2015), one may want to constrain the dispersion  $\sigma_{\text{broad}}$  of the broad emission component, if present, to be significantly larger than that  $\sigma_{\text{narrow}}$  of the narrow one, to avoid the degeneracy of fitting two similar lines. Or one may want to set the constraint  $\sigma_{\text{broad}} > \sigma_{\text{narrow}} + \Delta\sigma$ , or as a fractional difference  $\sigma_{\text{broad}} > f \times \sigma_{\text{narrow}}$ . Or one may want to constrain the velocity of a possible broad emission component not to differ more than a certain value from that of the narrow one  $|V_{\text{broad}} - V_{\text{narrow}}| < \Delta V$ . Efficiently setting this kind of constraint requires solving a constrained nonlinear optimization problem.

For maximum computational efficiency and accuracy, one should exploit the special problem that PPXF has to solve (Cappellari 2017, sec. 3.4). In particular, the function to minimize  $f(\mathbf{x})$  is a sum of squares and the typical constraints are linear. The problem to solve can be expressed as

$$\begin{aligned} \text{minimize } & f(\mathbf{x}) = \|\mathbf{r}(\mathbf{x})\|^2 \\ \text{subject to } & \mathbf{A}_{\text{eq}} \cdot \mathbf{x} = \mathbf{b}_{\text{eq}} \\ & \mathbf{A}_{\text{ineq}} \cdot \mathbf{x} \leq \mathbf{b}_{\text{ineq}}. \end{aligned} \quad (6)$$

I have searched extensively for a specialized algorithm that I could easily use in PPXF to efficiently solve this specific problem but did not find any. For this reason, I developed my own.

One of the most effective ways of solving nonlinear problems with general constraints is the sequential quadratic programming (SQP) method, where at every iteration the algorithm solves a constrained quadratic problem that approximates the function at the current location (e.g. Nocedal & Wright 2006, chap. 18).

In least-squares problems, one can approximate to second order the function near the current point  $\mathbf{x}_k$ , with  $\mathbf{p} = \mathbf{x} - \mathbf{x}_k$  (e.g. Nocedal & Wright 2006, sec. 10.2) as

$$f(\mathbf{x}) \approx \|\mathbf{J}_k \cdot \mathbf{p} + \mathbf{r}_k\|^2 \quad (7a)$$

$$= \mathbf{p} \cdot (\mathbf{J}_k^T \cdot \mathbf{J}_k) \cdot \mathbf{p} + 2\mathbf{p} \cdot (\mathbf{J}_k^T \cdot \mathbf{r}_k) + \|\mathbf{r}_k\|^2, \quad (7b)$$

$$\approx \mathbf{p} \cdot \nabla^2 f(\mathbf{x}) \cdot \mathbf{p} + 2\mathbf{p} \cdot \nabla f(\mathbf{x}) + \|\mathbf{r}_k\|^2, \quad (7c)$$

where  $\mathbf{J}_k$  is the Jacobian, which can be computed by finite differences,  $\nabla f(\mathbf{x}) = \mathbf{J}_k^T \cdot \mathbf{r}_k$  is the gradient and  $\nabla^2 f(\mathbf{x}) = \mathbf{J}_k^T \cdot \mathbf{J}_k$  is the *quasi-Newton* approximation of the Hessian, whose full form is the following, but I ignored the second term (e.g. Nocedal & Wright 2006, eq. 10.5)

$$\nabla^2 f(\mathbf{x}) = \mathbf{J}^T \cdot \mathbf{J} + \sum_{j=1}^m r_j \nabla^2 r_j. \quad (8)$$

It is a characteristic of least-squares problems that one can ap-

proximate the Hessian “for free” using  $\mathbf{J}$  and the reason it is important to adopt specialized methods for their solution. In the case of PPXF, the Hessian approximation is always especially good, even far from the solution, because the algorithm separates the linear and nonlinear optimization of the templates (sec. 3.3–3.4 of Cappellari 2017) and ensures that  $\sum_j r_j = 0$  at every step. This tends to cancel out the second term in the Hessian of equation (8).

In essence, a specialized SQP algorithm to solve equation (6) would consist of solving a sequence of quadratic sub-problems as follows

$$\begin{aligned} \text{minimize } & g(\mathbf{p}) = \|\mathbf{J}_k \cdot \mathbf{p} + \mathbf{r}_k\|^2 \\ \text{subject to } & \mathbf{A}_{\text{eq}} \cdot \mathbf{x} = \mathbf{b}_{\text{eq}} \\ & \mathbf{A}_{\text{ineq}} \cdot \mathbf{x} \leq \mathbf{b}_{\text{ineq}}. \end{aligned} \quad (9)$$

Algorithms for this type of problem are discussed e.g. by Fletcher (1987, sec. 11.2) or Gill et al. (1981, chapter 5). I implemented those ideas into a trust-region algorithm (Nocedal & Wright 2006, chap. 4) but I discovered that the approach is not sufficiently robust for my rather special situation.

The difficulty of the optimization problem I have to solve consists of the fact that the Jacobian can sometimes be completely degenerate. A common situation where this happens is when PPXF is fitting for the kinematics of emission lines or multiple stellar kinematic components. In this situation, the weights associated with a given emission line or stellar component may become exactly zero, because the line or component is simply not present in a certain galaxy spectrum. In other cases, the signal-to-noise ratio  $S/N$  may be too low to give any constraints to some parameters. In these cases, the gradient (column of  $\mathbf{J}$ ) with respect to the parameters describing the kinematics of the missing component will be zero.

I tried using the Singular Value Decomposition (SVD, e.g. Press et al. 2007, sec. 15.4.2) during the iterations required to solve the quadratic sub-problem. But after extensive testing, e.g. during the development of the MaNGA Data Analysis Pipeline (Westfall et al. 2019), I was unable to find a robust criterion to decide which singular values must be edited and find the effective rank of my Jacobian.

#### 3.2.2 The solution

To solve *unconstrained* least-squares optimization problems one of the most widely used techniques is the Levenberg-Marquardt (LM) method (Levenberg 1944; Marquardt 1963) and its state-of-the-art implementation in MINPACK (Moré 1978; Moré et al. 1980). The success of the LM method comes from the fact that the method penalizes the  $\mathbf{J}$  matrix defining the quadratic sub-problem in an adaptive fashion, in such a way that it always prevents degeneracy. This also makes the LM method a robust trust-region algorithms, as discussed in Fletcher (1987, sec. 5.2) or Nocedal & Wright (2006, sec. 10.3). Press et al. (2007, sec. 15.5.2) provides a less technical description.

In a previous version of PPXF, I used the LM algorithm, as modified in the MPFIT implementation by Markwardt (2009), which included a very useful but non-optimal treatment of box constraints (i.e. upper/lower limits on the parameters). Comparable box-constrained least-squares methods exist in Scipy (Virtanen et al. 2020) as implemented in the trust-region reflective algorithm (method='trf'; Branch et al. 1999) and the dogleg algorithm (method='dogbox', Voglis & Lagaris 2004, Nocedal & Wright 2006, chapter 4) in `scipy.optimize.least_squares`. These methods are available in PPXF but cannot support linear constraints.

After extensive experimentation with real-world cases, I imple-

mented a novel hybrid between the SCP and LM methods, specialized for the nonlinear least-squares with linear constraints (both equality and inequality). The algorithm consists of a trust-region quasi-Newton SCP method, with linear constraints, in which the matrix defining the quadratic sub-problem is penalized to avoid the risk of degeneracy, as in the LM method. I achieve this by replacing the quadratic sub-problem of [equation \(9\)](#) with the following (see [Nocedal & Wright 2006](#), eq. 10.41)

$$\begin{aligned} \text{minimize } g(\mathbf{p}) &= \left\| \begin{pmatrix} \mathbf{J}_k \\ \sqrt{\lambda_k} \mathbf{D}_k \end{pmatrix} \cdot \mathbf{p} + \begin{pmatrix} \mathbf{r}_k \\ 0 \end{pmatrix} \right\|^2 \\ \text{subject to } \mathbf{A}_{\text{eq}} \cdot \mathbf{x} &= \mathbf{b}_{\text{eq}} \\ \mathbf{A}_{\text{ineq}} \cdot \mathbf{x} &\leq \mathbf{b}_{\text{ineq}}, \end{aligned} \quad (10)$$

where  $\mathbf{D}_k$  is a diagonal matrix, which makes the problem scale invariant. By default, the diagonal elements of  $\mathbf{D}_k$  are initialized with the norm  $\|\cdot\|$  of the columns of  $\mathbf{J}$  and is updated during the iterations as suggested in [Moré \(1978, eq. 6.3\)](#). Close to the solution, when the quadratic model provides a good approximation of  $f(\mathbf{x})$ , then  $\lambda_k$  becomes small and [equation \(10\)](#) approximates [equation \(9\)](#). In this limit, the method behaves as an SCP method. When the quadratic approximation is inaccurate,  $\lambda_k$  becomes large and the method behaves as a trust-region LM method.

My resulting algorithm is rather simple because I did not worry about the efficiency of the solution of the quadratic programming sub-problem. The latter generally dominates the complexity of other state-of-the-art algorithms, which devise approximated matrix updates to save computation time (e.g. see the description of LM in [Moré 1978](#)). I also did not try to deal with large-scale problems and sparse matrices which also increase complexity and require specialized methods (e.g. [Gill et al. 2005](#)). Instead, I focused on the fitting of rather small nonlinear problems ( $n \lesssim 50$  variables) in which computing the function  $f(\mathbf{x})$  involves creating a complex model, as in PPXF. In this rather common situation, the time to solve the small quadratic programming sub-problem becomes negligible compared to that of evaluating  $f(\mathbf{x})$ . The solution is given in [Algorithm 2](#), which I implemented in the `capfit` procedure in the PPXF package.

#### Algorithm 2 CAPFIT: linearly constrained least-squares trust region

---

Given  $\mathbf{x}_1, \lambda > 0, \eta \in [0, 1/4]$   
 $\mathbf{r}_1 = f(\mathbf{x}_1)$   
 $\mathbf{J} = \mathbf{J}(\mathbf{x}_1)$   
Compute the scaling matrix  $\mathbf{D}$  » See text  
**loop**  
  Obtain  $\mathbf{p}$  as solution of [equation \(10\)](#) with  $\mathbf{J}, \mathbf{D}, \mathbf{r}_1, \lambda$   
   $\mathbf{x}_2 = \mathbf{x}_1 + \mathbf{p}$   
   $\mathbf{r}_2 = f(\mathbf{x}_2)$   
   $r_{\text{act}} = \chi^2(\mathbf{r}_1) - \chi^2(\mathbf{r}_2)$  » Using  $\chi^2(\mathbf{x}) \equiv \mathbf{x} \cdot \mathbf{x}$   
   $r_{\text{pre}} = \chi^2(\mathbf{r}_1) - \chi^2(\mathbf{J} \cdot \mathbf{p} + \mathbf{r}_1)$   
   $\rho = r_{\text{act}}/r_{\text{pre}}$  » Actual vs predicted reduction  
  **if** convergence test is satisfied **then**  
    **stop** with solution  $\mathbf{x}_2$   
  **if**  $\rho < 1/4$  **then**  
     $\lambda = 4\lambda$   
  **else if**  $\rho > 3/4$  **then**  
     $\lambda = \lambda/2$   
  **if**  $\rho > \eta$  **then** » Successful step: move on  
     $\mathbf{J} = \mathbf{J}(\mathbf{x}_2)$   
  Adjust the scaling matrix  $\mathbf{D}$  » See text  
   $\mathbf{x}_1, \mathbf{r}_1 = \mathbf{x}_2, \mathbf{r}_2$

---

Except for the fact that the quadratic sub-problem is linearly-

constrained, the algorithm uses the standard trust-region framework (e.g. [Nocedal & Wright 2006](#), algorithm 4.1, or [Fletcher 1987](#), algorithm 5.2.7). For the convergence criteria, I follow the description in [Moré et al. \(1980, sec. 2.3\)](#).

#### 3.2.3 Solving the quadratic sub-problem

I implemented two procedures to solve the quadratic programming sub-problem of [equation \(10\)](#). In both cases, I avoid explicitly constructing the Hessian  $\mathbf{J}_k^T \cdot \mathbf{J}_k$  as this would degrade the conditioning of the system. The first procedure (`lsq_box`) is specialized for the common situation where only box constraints are present. It solves  $\min \|\mathbf{A} \cdot \mathbf{x} - \mathbf{b}\|^2$  with  $\mathbf{lb} < \mathbf{x} < \mathbf{ub}$ . For this, I use the active-set method adopted in the non-negative least-squares (NNLS) method ([Lawson & Hanson 1995](#), algorithm 23.10), which was generalized for box constraints with the Bounded-Variables Least-Squares (BVLs) procedure in the same book and in [Stark & Parker \(1995\)](#). My implementation closely follows [Lawson & Hanson \(1995\)](#) except for the important fact that (i) I allow for a starting guess and (ii) I include an initialization step ([Algorithm 3](#)) which generalizes to the box constrained case the initialization loop in the `FASTNNLS` code<sup>4</sup> by [Andersson & Bro \(2000\)](#). In realistic PPXF problems, using my new `lsq_box` with hundreds of spectral templates produced a typical speedup of a factor four compared to using the `scipy.optimize.nnls`, which is a wrapper to the [Lawson & Hanson \(1995\)](#) Fortran code. The procedure `scipy.optimize.lsq_linear` currently also does not support passing a starting guess.

---

#### Algorithm 3 Initialization `lsq_box` box-constrained least-squares

Given  $\mathbf{x}$ , lower  $\mathbf{lb}$  and upper  $\mathbf{ub}$  bounds,  $\mathcal{B} \neq \emptyset$   
**while**  $\mathcal{B} \neq \emptyset$  **do**  
   $\mathcal{B} = \{\mathbf{x} \mid (\mathbf{x} < \mathbf{lb}) \vee (\mathbf{ub} < \mathbf{x})\}$   
  Set all  $\mathbf{x} \in \mathcal{B}$  to the nearest bound  
   $\mathcal{F} = \{\mathbf{x} \mid \mathbf{lb} < \mathbf{x} < \mathbf{ub}\}$   
   $\mathbf{x}' = \min \|\mathbf{A} \cdot \mathbf{x} - \mathbf{b}\|^2$  for  $\mathbf{x} \in \mathcal{F}$   
  Set  $\mathbf{x} = \mathbf{x}'$  for  $\mathbf{x} \in \mathcal{F}$

---

The second procedure (`lsq_lin`) solves general linearly-constrained quadratic programming problems like in [equation \(9\)](#) using a modified version of the standard active-set technique described by [Nocedal & Wright \(2006, algorithm 16.3\)](#). The approach consists of solving a sequence of equality-constrained linear least-squares problems, for which I follow [Golub \(2013, algorithm 6.2.2\)](#), allowing for degenerate matrices using SVD. If the initial guess is unfeasible, I find a feasible point using the linear programming procedure `scipy.optimize.linprog` and the `method='highs'` by [Huangfu & Hall \(2017\)](#). Alternatively, the quadratic sub-problem can be solved within PPXF by minimizing the quadratic function in the form of [equation \(7b\)](#) using a general interior-point quadratic programming solver within the `cvxopt` package<sup>5</sup> by [Andersen et al. \(2011\)](#). The latter is much faster for large-scale problems. I have extensively tested the `lsq_box` and `lsq_lin` procedure described in this section by constructing batteries of tests using both exact analytic solutions and comparisons against `cvxopt`.

The `capfit` procedure has been the default nonlinear optimization algorithm in PPXF for about three years and has been used as a general optimizer independently of PPXF too. During this time PPXF was used to fit millions of spectra from a variety of surveys (e.g.

<sup>4</sup> Available from <http://www.models.kvl.dk/nwaytoolbox>

<sup>5</sup> Available from <https://cvxopt.org/>

MaNGA [Bundy et al. 2015](#) and SAMI [Bryant et al. 2015](#)). This allows me to fix its handling of rare failures in degenerate situations, which are difficult to encounter in idealized examples. When applied to unconstrained least-squares problems `capfit` produces essentially the same iterates as the state-of-the-art LM implementations in `minpack` or `mpfit`, as expected. When used for box-constrained least-squares problems `capfit` is generally at least as efficient as the best algorithms in `scipy.optimize.least_squares`. However, `capfit` allows for the extra flexibility of using linear constraints, as well as for keeping variables tied to others or fixed.

### 3.3 Setting linear constraints on the template weights

In the previous section, I discussed the use of linear constraints on the kinematic parameters during the `ppxf` fit. Here I note that linear constraints can be used also during the linear-fitting procedure in [Cappellari \(2017, sec. 3.3\)](#). These were used for example to constrain the sum of weights (e.g. the luminosity) of different template groups to constitute a certain fraction of the total light, e.g. to perform kinematic bulge/disks decompositions (e.g. [Tabor et al. 2017, 2019; Oh et al. 2020](#)) or to study stellar population of different kinematic components (e.g. [Shetty et al. 2020](#)).

### 3.4 Multi-dimensional regularization

Considering without loss of generality that stellar population depends only on age, the fundamental equation used to model the spectrum of a composite stellar population is (e.g. [Cid Fernandes et al. 2005; Ocvirk et al. 2006; Conroy 2013, sec. 2.3](#))

$$G_{\text{mod}}(\lambda) = \int_{t=0}^{t=T} \text{SSP}_\lambda(t, Z) \cdot \text{SFR}(T - t) \, dt, \quad (11)$$

where  $\text{SFR}$  is the star formation rate,  $\text{SSP}_\lambda$  is a Single Stellar Population spectrum per unit mass, with age  $t$  and metallicity  $Z$ , while  $T$  is the age of the Universe at the redshift of the galaxy. This expression is generalized in `ppxf` to study the distribution of more parameters, like e.g. metallicity,  $\alpha$  enhancement or IMF, in addition to the SFR.

I pointed out in [Cappellari \(2017, sec. 3.5\)](#) that [equation \(11\)](#) is an inhomogeneous Fredholm equation of the first kind, with kernel  $\text{SSP}_\lambda$ . And the recovery of the  $\text{SFR}(t)$  from the observed  $G_{\text{mod}}$  is a textbook example of ill-conditioned inverse problem (e.g. [Hansen 1998; Kabanikhin 2011; Press et al. 2007, sec. 19.0](#)). This means that one cannot find a unique solution from real data without further assumptions.

In [Cappellari \(2017, sec. 3.5\)](#) I discussed the implementation of linear regularization (e.g. [Press et al. 2007, sec. 19.5](#)) in `ppxf` to address this issue and study the stellar population in galaxies. I gave a formula for the second-order one-dimensional regularization. Given that there are alternative ways of generalizing a measure of smoothness of a function in dimension larger than one (e.g. [Brady & Horn 1983](#)), I clarify here that the second-order regularization (`reg_ord=2`) in `ppxf` minimizes the total squared Laplacian ( $\Delta w$ )<sup>2</sup> of the weights  $w$  distribution, while the first-order one (`reg_ord=1`) minimizes the total squared gradient ( $\nabla w$ )<sup>2</sup>. Both operators are implemented by standard finite differences.

[Press et al. \(2007, 19.4.1\)](#) point out that, under some sensible conditions, the regularized solution has a simple Bayesian interpretation: it represents the most likely solution for the weights, given an adjustable prior on the amplitude of the fluctuations. However, the meaning of the fundamental degeneracy of the stellar population inversion, as well as of regularization, is best illustrated with an example.

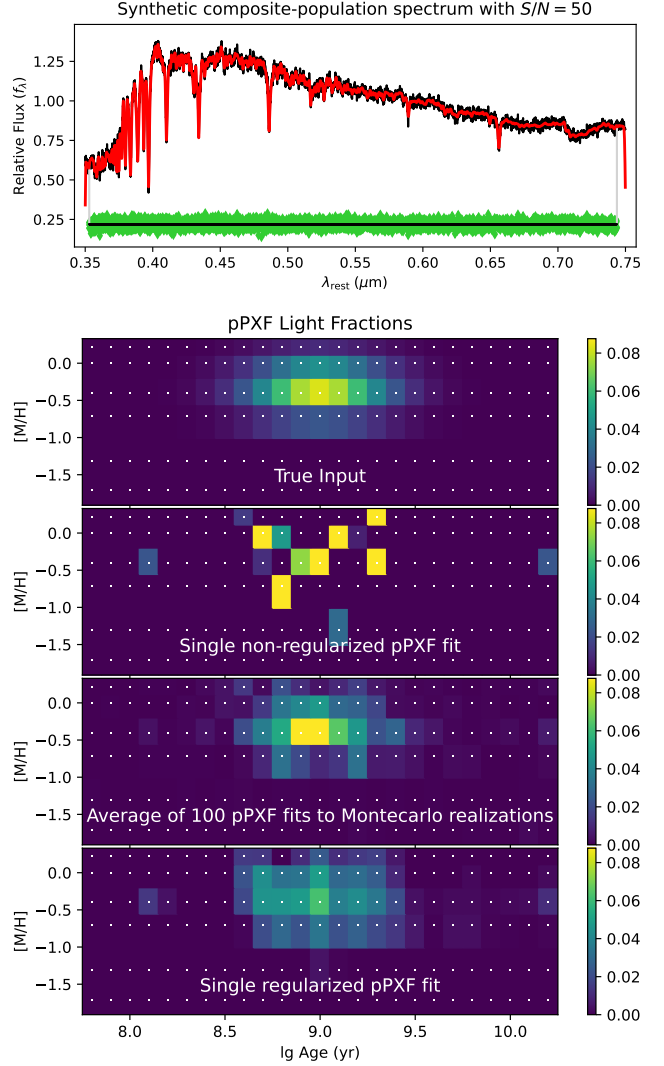


**Figure 1.** Top panel: synthetic input spectrum with Gaussian noise at  $S/N = 50$ . Second panel: input distribution of the  $V$ -band templates luminosity. Third panel: recovered weights from a single non-regularized `ppxf` fit to one Monte Carlo realization of the noise. Fourth panel: average of the weights recovered with `ppxf` by fitting 100 Monte Carlo realizations of the synthetic spectrum. Bottom panel: weights recovered with a single `ppxf` fit with regularization `regul=30`.

I used a grid of 25 logarithmically-spaced ages  $t$  and 6 metallicities  $[M/H]$  from the SPS models by [Vazdekis et al. \(2015\)](#) to construct a synthetic spectrum in which the distribution of light contributed by each spectrum in the  $V$  band follows a bivariate Gaussian distribution  $\mathcal{N}(t, [M/H])$  with mean age  $t_0 = 1$  Gyr, mean  $[M/H]_0 = -0.3$  and dispersion of 0.25 dex in both age and metallicity. I logarithmically sampled the spectrum at a velocity scale  $\Delta V = c \Delta \ln \lambda = 50 \text{ km s}^{-1}$  per spectral pixel.

I show the resulting spectrum in the top panel of [Fig. 1](#) and the input light-weights distribution in the second panel. The third panel shows a single `ppxf` fit, which is characterized by discrete sharp peaks as expected due to the ill-conditioning of the inversion problem. The fourth panel shows the result of averaging the weights obtained by fitting with `ppxf` 100 Monte Carlo realizations obtained by adding Gaussian noise on the same noiseless synthetic spectrum.

Here, the average converges towards the true input distribution. Finally, in the bottom panel I show the result of performing a single regularized PPXF fit (with `reg_order=2` and a typical `regul=30`). Here the distribution looks comparable to that of the average of multiple realizations.

Regularization has its limitations, in fact, it is by construction a trade-off between agreement with the data and smoothness (e.g. Press et al. 2007, fig. 19.4.1), which may introduce biases. In general, when one is obtaining results by averaging many spectra, it may be better not to use regularization, or only use a minimal amount, to reduce possible biases, while allowing the differences in the noise between spectra to act as Monte Carlo realizations. But regularization is very useful when interpreting individual spectral fits and even to reduce noise in the SPS models themselves, which may introduce spurious features in the solutions (as I found later).

One can use bootstrapping of the residuals, while repeating the PPXF fits multiple times, to obtain averages as well as uncertainties in the distribution of the weights as done e.g. by Kacharov et al. (2018, figs. 8–13). In this case, it is important to perform the initial PPXF fit, from which the residuals are extracted, using some regularization, to obtain a less noisy and more representative best fitting spectrum. I achieved good results perturbing the residuals using the easy-to-use wild bootstrap method (Davidson & Flachaire 2008).

### 3.5 Global nonlinear fitting

In the most common situations, e.g. when fitting a single stellar kinematic component with emission lines, the spectral fitting problem has a single global minimum and the local optimization method of Section 3.2 is guaranteed to efficiently converge to it. However, in more complex situations, like when fitting multiple stellar or gas kinematic components, the fitting problem may present multiple minima and a local optimizer is not guaranteed to converge to the global minimum.

The standard way of dealing with multiple minima in PPXF is to perform the optimization of the variables in which the  $\chi^2$  function is multi-modal outside of PPXF, while calling PPXF with those variables fixed, from inside a wrapper function. For example, when studying multiple kinematic components one may sample a grid of velocities and call PPXF with fixed velocities at every location (e.g. Mitzkus et al. 2017; Tabor et al. 2017; Bevacqua et al. 2022). If one is interested in the full posterior of certain parameters, and computation time is not an issue, one may call PPXF with those parameters fixed from within a Bayesian method like MultiNest (Feroz et al. 2009), EMCEE (Foreman-Mackey et al. 2013), AdaMet (Cappellari et al. 2013a) or DYNESTY (Speagle 2020), assuming the contribution of the fitted parameters to the posterior can be neglected.

In the current version of PPXF one can also perform the global optimization within PPXF. This is currently implemented using the function `scipy.optimize.differential_evolution`, which uses the Differential Evolution algorithm by Storn & Price (1997). The Scipy function allows for linear constraints using the method by Lampinen (2002). To save computation time, by default I do not run the global optimization step until convergence, but I use it as starting point for the usual CapFitt procedure.

An example of a situation where using both the global optimization and the linear constraints options can be useful, and the corresponding PPXF fit is shown in Fig. 2. The plots show the central spectrum of the active galaxy NGC 1386, extracted from the MUSE (Bacon et al. 2010) integral-field spectroscopic observations presented in Venturi et al. (2021). The emission line spectrum clearly requires at least three distinct kinematic components (see also Lena et al.

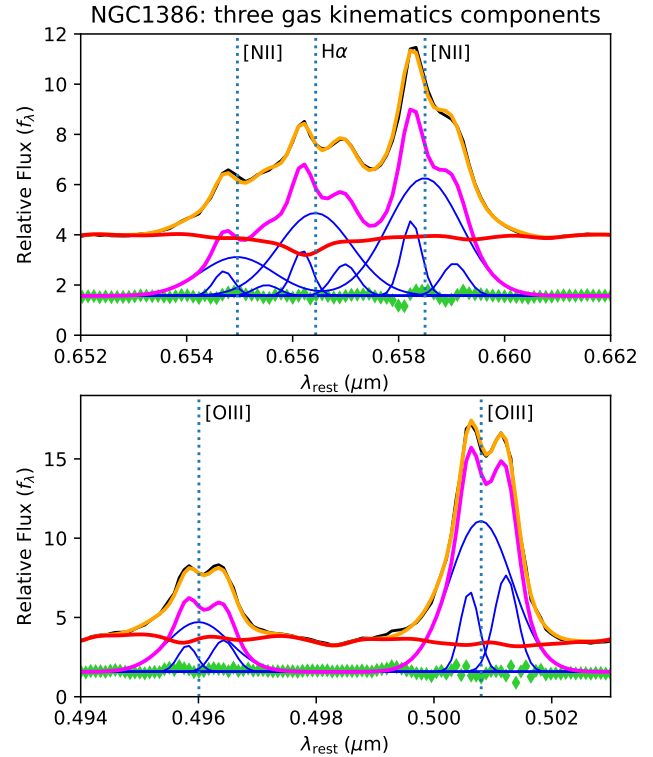


**Figure 2.** Fit of a MUSE spectrum of the active galaxy NGC 1386 (thin black line, mostly hidden by the fit), using the global optimization option (`global_search=True`) and linear constraints (`constr_kinem`) in PPXF. Each of the five emission lines is modelled with three kinematic components (see text). The orange line is the PPXF total best fit, the red line is the best fitting stellar spectrum alone, while the magenta is for the gas emissions alone, with individual components shown in blue. The fit residuals are shown with green diamonds. I only plot the region with the key emissions, but I fitted the full optical spectrum, which is needed to constrain the stellar contribution.

2015). The definition of the three kinematics components may appear ill-defined, due to the extensive blending of the lines. However, a meaningful decomposition can be obtained with some simple assumptions. Here I required the kinematics ( $V, \sigma$ ) of all five emission lines to be the same within each of the three kinematic components. I additionally required the  $\sigma_{\text{broad}}$  of the broad component to be at least  $200 \text{ km s}^{-1}$  broader than either of the two narrow components as follows  $\sigma_{\text{broad}} > \sigma_{\text{narrow},1}$  and  $\sigma_{\text{broad}} > \sigma_{\text{narrow},2}$ . These are linear constraints that I enforced using the `constr_kinem` keyword in PPXF.

### 3.6 Fitting spectra and photometry

Including photometry in a full-spectrum fitting method is conceptually equivalent to simply including in the fit a few extra pixels, corresponding to the fluxes measured in a set of observed photometric bands. The two differences are (i) that the photometric fluxes do not depend on the line-of-sight velocity-distribution (LOSVD)  $\mathcal{L}_n(v)$  like the spectroscopic ones and (ii) the photometry of an individual galaxy is generally unable to constrain both the calibration inaccuracies and the template weights. This implies that one cannot include polynomials as done for the spectroscopy.

I define a function that describes an individual template spectrum  $T_n(\lambda)$  (either stars or gas), convolved  $*$  with the LOSVD, which is

allowed to be different for each template

$$g_n(\lambda) = T_n(\lambda) * \mathcal{L}_n(\nu). \quad (12)$$

With this notation, the model for the galaxy spectrum becomes

$$G_{\text{mod}}^{\text{spec}}(\lambda) = \sum_{n=1}^N w_n \left[ g_n(\lambda) A_n(\lambda) \sum_{k=1}^K a_k \mathcal{P}_k(\lambda) \right] + \sum_{l=0}^L b_l \mathcal{P}_l(\lambda) + \sum_{j=1}^J c_j S_j(\lambda), \quad (13)$$

where the  $\mathcal{P}_k$  and  $\mathcal{P}_l$  are multiplicative and additive polynomials respectively (of Legendre or trigonometric type) and the  $S_j$  are optional spectra of the sky. This model is nearly the same as in Cappellari (2017, eq. 11), except for the fact that here each template spectrum can have a different attenuation function  $A_k$ . Moreover, both the attenuation and multiplicative polynomials can be used at the same time, rather than being alternatives. This is especially useful when including photometry in the fit, which removes the degeneracy between the attenuation curve and the multiplicative polynomials.

The model for the photometric measurements, in linear units, not magnitudes, is given by the following expression

$$G_{\text{mod}}^{\text{phot}}(\lambda_q) = \sum_{n=1}^N w_n \langle g_n(\lambda) A_n(\lambda) \rangle_q, \quad (14)$$

where  $\langle \cdot \rangle_q$  represents the mean flux in the  $q$ -th photometric band with effective wavelength  $\lambda_q$ . Unlike the spectroscopic model of equation (13), the photometric model of equation (14) does not include polynomials or the sky spectrum.

In the common case of an energy-integrating detector, and assuming fluxes as  $f_\lambda$  (e.g. in units of  $\text{erg cm}^{-2} \text{ s}^{-1} \text{ \AA}^{-1}$ ) the mean flux is given by (e.g. Bessell & Murphy 2012, eq. A11)

$$\langle f_\lambda \rangle_q = \frac{\int f_\lambda(\lambda) S_q(\lambda) \lambda d\lambda}{\int S(\lambda) \lambda d\lambda}, \quad (15)$$

where  $S_q(\lambda)$  is the system photon response function and the integral extends over the region where  $S_q$  is nonzero. Alternative expressions can be used when the fluxes were measured differently.

In the common situation in which the covariance between the spectroscopic  $G^{\text{spec}}$  or photometric  $G^{\text{phot}}$  measurements are not known, or ignored, the residuals  $\mathbf{r}$  from the fit are as in Cappellari (2017, eq. 22)

$$r_p = \frac{G_{\text{mod}}^{\text{spec}}(\lambda_p) - G^{\text{spec}}(\lambda_p)}{\Delta G^{\text{spec}}(\lambda_p)}, \quad p = 1, \dots, P \quad (16a)$$

$$r_q = \frac{G_{\text{mod}}^{\text{phot}}(\lambda_q) - G^{\text{phot}}(\lambda_q)}{\Delta G^{\text{phot}}(\lambda_q)}, \quad q = P + 1, \dots, P + Q, \quad (16b)$$

with the difference that the vector of residuals now includes both the  $P$  spectroscopic and the  $Q$  photometric values. In other words, the total  $\chi_{\text{total}}$  from the fit, which is proportional to the log-likelihood  $\ln \mathcal{L}$ , now becomes the sum of the spectroscopic and photometric ones

$$\chi_{\text{total}} = \chi_{\text{spec}} + \chi_{\text{phot}}. \quad (17)$$

Both the linear and nonlinear fit, the regularization and the possible treatment of covariances, proceed unchanged as already described in Cappellari (2017, sec. 3.3–3.5). The only difference is one extra row in the matrix  $\mathbf{A}$ , defined in (Cappellari 2017, sec. 3.3), for every photometric measurement.

According to the mean value theorem for integration, for every  $q$ -th band and  $n$ -th template there exists a wavelength  $\lambda_{q,n}$  which satisfies

$$A_n(\lambda_{q,n}) \langle g_n(\lambda) \rangle_q = \langle g_n(\lambda) A_n(\lambda) \rangle_q. \quad (18)$$

When one has a good estimate of the galaxy redshift (e.g. from previous photometric redshift), or when performing a grid search for the best-fitting redshift, the redshift of the spectrum changes little. This makes the quantities  $\langle g_n(\lambda) \rangle_q$  essentially independent of  $\mathcal{L}_n(\nu)$  during a fit. If I rewrite equation (14) as

$$G_{\text{mod}}^{\text{phot}}(\lambda_q) = \sum_{n=1}^N w_n A_n(\lambda_{q,n}) \langle g_n(\lambda) \rangle_q, \quad (19)$$

I can precompute the  $\langle g_n(\lambda) \rangle_q$  for all templates before the fit. This approach can make the computation time when adding photometry to a fit insignificant compared to the fitting of the spectrum alone.

A good approximation for the wavelength satisfying equation (18) is (e.g. Bessell & Murphy 2012, eq. A21)

$$\lambda_{q,n} = \frac{\int g_n(\lambda) S_q(\lambda) \lambda^2 d\lambda}{\int g_n(\lambda) S_q(\lambda) \lambda d\lambda}. \quad (20)$$

### 3.7 Dust attenuation

As illustrated in equation (13) and equation (14), in the new ppXF method each template can be associated with a different attenuation curve. In practice, one is expected to use this feature to vary the attenuation curve only for specific groups of templates.

According to our current understanding of the attenuation by dust in galaxies (see review by Salim & Narayanan 2020), one expects to be useful to distinguish three groups of attenuation curves (i) for the very young population of stars (with typical ages  $t \lesssim 10^7$  yr), when they are assumed to be still embedded into their birth cloud (Charlot & Fall 2000; Granato et al. 2000); (ii) for the whole stellar population (both young and old), due to diffuse dust and (iii) for the gas emission lines produced in star-forming regions.

In ppXF one can adopt a generic function, which can be different for different templates and can have an arbitrary number of parameters. The parameters can have bounds or can be kept fixed. By default I currently implemented a four-parameters attenuation function  $A(\lambda) = f(A_V, \delta, E_b, f_{\text{nodust}})$  defined by

$$D(\lambda) = \frac{E_b (\lambda \Delta \lambda)^2}{(\lambda^2 - \lambda_0^2)^2 + (\lambda \Delta \lambda)^2} \quad (21a)$$

$$k(\lambda) = \frac{A_V}{R_V} [k'(\lambda) + D(\lambda)] \left( \frac{\lambda}{\lambda_V} \right)^\delta \quad (21b)$$

$$A(\lambda) = f_{\text{nodust}} + (1 - f_{\text{nodust}}) 10^{-0.4 k(\lambda)}. \quad (21c)$$

Here equation (21a) is the Lorentzian-like Drude function adopted by Noll et al. (2009) to describe the UV bump around  $\lambda_0 = 0.2175 \mu\text{m}$ , with a width  $\Delta\lambda = 0.035 \mu\text{m}$ . The equation (21b) is the expression adopted by Kriek & Conroy (2013), which includes the attenuation  $k'(\lambda)$  and  $R_V = 4.05$  from Calzetti et al. (2000, eq. 4 and 5), and allows for a variable UV slope  $\delta$  around the pivot  $V$ -band wavelength  $\lambda_V = 0.55 \mu\text{m}$ . Optionally, one can make  $E_b$  a function of  $\delta$  as in Kriek & Conroy (2013, eq. 3). Finally equation (21c) allows one to specify the fraction  $f_{\text{nodust}}$  of stellar population (for the given template) that is unattenuated, as suggested by Lower et al. (2022). The resulting  $A(\lambda)$  is the factor to multiply the template at the given wavelength to model the attenuation effect.

## 4 DATA AND SPS MODELS

In the rest of this paper, I present an analysis of the combined photometric and spectroscopic data, for a sample of about 3200 galaxies at  $0.6 < z < 1$ , making use of various of the new features of ppXF introduced in the first part of the paper.

## 4.1 Spectroscopy

I study a subset of the galaxy sample of the LEGA-C survey (van der Wel et al. 2016). It is an ESO ESO/Very Large Telescope (VLT) public spectroscopic survey targeting galaxies in the redshift range  $0.6 < z < 1$ , selected based on their observed  $K_s$ -band luminosity in the UltraVista/COSMOS catalogue by Muzzin et al. (2013), with a small variation of the  $K_s$  limit with  $z$ . In this work, I use the data from the LEGA-C third data release (DR3) presented in van der Wel et al. (2021). This redshift selection results in a mass-complete sample of 3445 galaxies in DR3 (90% completeness above  $\lg(M_*/M_\odot) \gtrsim 10.3$ ). The selection, the completeness level, the characteristics of the sample and the data reduction are discussed extensively in van der Wel et al. (2016) and Straatman et al. (2018).

For my study, I focused only on the subsample of 3197 galaxies in the DR3 catalogue with spectroscopic redshift  $0.6 < z < 1$  and with measured stellar velocity dispersion  $\sigma_*$ . This a sample has redshift  $z = [0.67, 0.76, 0.93]$  at the 16th ( $-1\sigma$ ), 50th (median) and 84th ( $+1\sigma$ ) percentiles. However I verified that all my results are unchanged if I restrict the sample to the redshift range to  $0.7 < z < 0.9$ .

The survey data consist of spectra observed with the VLT/VIMOS multi-object spectrograph (Le Fèvre et al. 2003) covering the wavelength range 0.63–0.88  $\mu\text{m}$  with a spectral resolution  $R \approx 3500$ , equivalent to an instrumental dispersion  $\sigma_{\text{inst}} \approx 36 \text{ km s}^{-1}$  (van der Wel et al. 2021). For the PPXF fits I logarithmically rebinned the spectra to a velocity scale  $\Delta V = c\Delta \ln \lambda = \sigma_{\text{inst}}$  (Cappellari 2017, eq. 8) to make sure the spectrum is Nyquist sampled.

## 4.2 Photometry

I use two large collections of photometric measurements for the LEGA-C galaxies. The first is the UltraVista/COSMOS catalogue by Muzzin et al. (2013). It includes PSF-matched photometry in 30 bands from 0.15 to 24  $\mu\text{m}$ . The catalogue is based on the  $YJHK_s$  NIR imaging data from UltraVISTA (McCracken et al. 2012). The optical data consist of broad-band Subaru/SuprimeCam data ( $g^+r^+i^+z^+B_jV_j$ ), as well as  $u^*$  data from the CFHT/MegaCam (Taniguchi et al. 2007; Capak et al. 2007). It also includes the 12 optical medium bands (IA427–IA827) from Subaru/SuprimeCam (Capak et al. 2007). Also included are the GALEX FUV and NUV channels (Martin et al. 2005), and the 3.6  $\mu\text{m}$  4.5  $\mu\text{m}$  5.8  $\mu\text{m}$  8.0  $\mu\text{m}$  and 24  $\mu\text{m}$  channels from Spitzer’s IRAC+MIPS cameras (Sanders et al. 2007).

The second photometric catalogue is the COSMOS2020 by Weaver et al. (2022). Highlights of this catalogue, compared to the one by Muzzin et al. (2013), are much deeper Subaru Hyper Suprime-Cam *grizy* broadband photometric measurements (Aihara et al. 2019) and deeper UltraVISTA DR4 observations  $YJHK_s$ . The extra depth is not an important feature for my study, as the LEGA-C galaxies were all well-detected in Muzzin et al. (2013) by design. However, I use the COSMOS2020 to assess the sensitivity of my results to the use of independent datasets. For this work, I adopt the catalogue produced with THE FARMER profile-fitting photometric extraction tool. I still extend that catalogue with the GALEX photometry, properly scaled, which is important to constrain the youngest component.

For both photometric catalogues, I only included the typically 28 bands which have a transmission FWHM fully contained in the wavelength range of the adopted stellar population templates (see later) at the redshift of each galaxy.

## 4.3 Stellar population synthesis models

I used three independent SPS models to assess the sensitivity of the results to some of the adopted model assumptions. I selected the models based on two criteria (i) the ability to generate model spectra from the far UV at 0.1  $\mu\text{m}$  to 2.5  $\mu\text{m}$ , to be able to constrain the decrease of  $f_\lambda$  towards the NIR region of the galaxy spectra and (ii) to include model spectra down to a young age of 1 Myr, to reproduce the many actively star-forming galaxies that are present in the sample. The age criterion forces me to exclude from this study the models by Vazdekis and Maraston, which I have extensively used in the past.

The three SPS models that satisfy my requirement and that I adopted are (i) the `fsps`<sup>6</sup> (Conroy et al. 2009; Conroy & Gunn 2010), (ii) the `GALAXEV`<sup>7</sup> (Bruzual & Charlot 2003) and (iii) the `BPASS`<sup>8</sup> SPS models (Stanway & Eldridge 2018; Byrne et al. 2022).

For all three models, I tried to select a consistent set of templates. In all cases, I adopted the same set of 43 ages logarithmically spaced by 0.1 dex from 1 Myr to 15.85 Gyr, defined as

$$\lg(\text{Age/yr}) = 6, 6.1, 6.2, \dots, 10.2. \quad (22)$$

The oldest age is much older than the age of the Universe at the redshift of the sample, which varies in my standard cosmology from 5.75 – 7.75 Gyr between  $z = 1 – 0.6$ , but I did not truncate the models to physical ages, to check how well the data themselves can constrain the galaxy ages. I also excluded from all models the most extreme low metallicities  $[Z/H] < -2$ . Here is my other setup for the three SPS:

(i) **The `fsps` models** allow one to compute SPS models for a specified set of parameters. I used the Python bindings<sup>9</sup> (Johnson et al. 2021a) and the latest public v3.2 to compute a set of spectra with the above ages and 9 equally-spaced metallicities  $[Z/H] = [-1.75, -1.5, -1.25, -1, -0.75, -0.5, -0.25, 0, 0.25]$ . I adopted a Salpeter (1955) IMF with an upper mass cut of  $100M_\odot$  for consistency with `BPASS`. But I note that my results are virtually insensitive to the slope of the IMF at lower masses. I computed the SPS without including the effect of gas or dust and adopted default parameters for the other parameters. This returns SPS spectra computed using the MILES stellar library (Sánchez-Blázquez et al. 2006; Falcón-Barroso et al. 2011) for the optical region, which is the one I fit in the LEGA-C spectra.

(ii) **The `GALAXEV` models** provide a Fortran code (version 2020) which I used to produce a set of SPS spectra with the same ages as above and computed at the provided 5 metallicities  $[M/H] = [-2.34, -1.74, -0.73, -0.42, 0, 0.47]$ . This SPS model also uses the MILES library to generate spectra of the optical region. Also here I adopted a Salpeter IMF.

(iii) **The `BPASS` models** v2.3 are provided as a set of files pre-computed at a given set of metallicity. I adopted the 10 metallicities<sup>10</sup>  $[Z/H] = [-1.3, -1, -0.8, -0.7, -0.5, -0.4, -0.3, 0, 0.2, 0.3]$ . The models are provided for a single IMF having a power slope -2.35 (Salpeter slope) above  $M > 0.5M_\odot$  and slope -1.3 at lower masses. I used the version of the SPS for single stars, ignoring binaries, with  $[\alpha/Fe] = 0$ , for consistency with the other two SPS models. These SPS models are fully synthetic.

<sup>6</sup> Available from <https://github.com/cconroy20/fsps>

<sup>7</sup> Available from <http://www.bruzual.org/bc03/>

<sup>8</sup> Available from <https://bpass.auckland.ac.nz/>

<sup>9</sup> Available from <https://github.com/dfm/python-fsps>

<sup>10</sup> The models are specified in metal mass fraction  $Z$ , and I converted it to  $[Z/H]$  with  $\sim 10\%$  accuracy.

## 5 SETUP FOR PPXF AND TESTS

In this study, fitting (twice) the VIMOS spectrum ( $\approx 2800$  spectral pixels) and typically 28 photometric bands for a single galaxy with PPXF takes about 1 min. This compares with the "roughly 100 CPU hours" reported by Tacchella et al. (2022) in a similar state-of-the-art study using DEIMOS spectroscopy and the PROSPECTOR Bayesian code (Johnson et al. 2021b). This is a computation time difference of nearly four orders of magnitude! Of course, the two methods perform quite different tasks and the large computational cost is a standard feature of Bayesian methods and not a weakness by itself. However, the execution time of a method affects the kind of tasks one can address and the variety of modelling choices one can explore as I outline in this section.

### 5.1 Non-parametric population model

A key feature made possible by least-squares methods is the ability to explore non-parametrically the joint distribution of SFH and chemical composition with high resolution. My setup uses 43 non-parametric age bins, and each age bin is allowed to have a different non-parametric metallicity (5 – 10 bins depending on the SPS code) for a total of up to 430 bins. This contrast with the 10 non-parametric age bins and the single parametric metallicity distribution for the entire galaxy adopted by Tacchella et al. (2022). Crucially, even when using a non-parametric grid of a few hundred templates the least-squares method *guarantees* global convergence to the most likely weights distribution. This is because the constrained quadratic-programming problem being solved (Cappellari 2017, eq. 27) is known to possess a unique global minimum (e.g. Nocedal & Wright 2006). This contrast with Bayesian methods, where Tacchella et al. (2022, sec. 3.2) reported that "the fits do not converge within a reasonable amount of time" with 14 non-parametric bins. The use of non-parametric models is important for a proper recovery of the stellar population in galaxies (Lower et al. 2020).

### 5.2 Polynomials

A least-squares method like PPXF allows for a quick exploration of different modelling assumptions. In the course of this study I was able to easily test different options, each with all three SPS models, for all 3200 galaxies, to test how they affected the final results. In particular, I run models with both multiplicative and additive polynomials degree from `mdegree=degree=-1` (i.e. using only attenuation and no polynomials) to degree 4 and found that the solution changes slightly without polynomials but quickly stabilizes as soon as one allows for a nonzero degree. Results were similar when only using additive or only multiplicative polynomial to adjust the spectral stellar continuum. This was a non-obvious result in the present analysis, given that the LEGA-C spectra were calibrated using SPS models (van der Wel et al. 2021) and this non-standard calibration may leave an influence on the results. The polynomials should effectively remove any memory of possible inaccuracies in the spectral calibration. I adopted the PPXF keywords `mdegree=2`, `degree=-1` for my standard setup.

### 5.3 Dust attenuation model

I truncated all three the SPS templates to  $0.01 \mu\text{m} < \lambda < 5 \mu\text{m}$  (except for the `bpass` SPS which only extend to  $\lambda < 2 \mu\text{m}$ ) to remove the influence of dust on the spectral shape (e.g. Conroy 2013, fig. 1). This is because the modelling of dust from the energy balance of

UV light reradiated to the IR requires several further assumptions and is not implemented in all modelling codes. Moreover, the currently available bands are included in the fitted range anyway. This situation is changing rapidly with the James Webb Space Telescope (JWST) and will soon be revisited.

For the full set of 3200 galaxies, I experimented with three different assumptions for the attenuation: (i) I adopted a single four-parameters attenuation for all stellar templates as in equation (21); (ii) I reduced the attenuation curve to two parameters ( $A_V, \delta$ ) by assuming  $f_{\text{nodust}} = 0$  and adopting the  $E_b - \delta$  relation by Kriek & Conroy (2013, eq. 3); I still applied this attenuation for all stellar templates; (iii) I adopted the two-components attenuation model by Charlot & Fall (2000). For this I used a birth-cloud attenuation of the form

$$k(\lambda) = A'_V \left( \frac{\lambda}{0.55 \mu\text{m}} \right)^{-1}. \quad (23)$$

I apply this only to the stellar templates younger than 10 Myr, while I used the same attenuation as in (ii) for the diffuse dust component affecting all stellar templates. In all three cases, I fit a different Calzetti et al. (2000) attenuation curve (equation (21) with  $E_b = \delta = f_{\text{hogas}} = 0$ ) for the gas emission lines templates.

I found that options (i) and (ii) produce an insignificant difference in the final results, but there is some degeneracy in the attenuation parameters, which makes any trend between dust parameters less obvious. Option (iii) generates a similar result for the older and intermediate populations, as expected. However, when allowing the youngest population to have its own attenuation, this becomes completely degenerate with the amount of star formation in that same young component. As a result, one can obtain good fits with an unlikely large attenuation associated with an equally large star formation, but with complete degeneracy between the two parameters. This is the well-known SFR-dust degeneracy mentioned in Section 1. It can be broken by introducing extra assumptions on the dust geometry and reradiated UV fraction, combined with rest-frame IR data, which I do not have.

In conclusion, I adopted as my standard choice the two-parameters attenuation function of the option (ii), which applies to the whole population, as done e.g. by Kriek & Conroy (2013). I enforced bounds on the parameters as  $-1 < \delta < 0.4$  and  $0 < A_V < 4$ .

### 5.4 Matching photometry and spectra

For every galaxy, I have a spectroscopic redshift from the LEGA-C catalogue and I only included a photometric band in the fit if the band FWHM is fully enclosed by the template's wavelength coverage at that redshift. I pre-computed the  $\langle g_n(\lambda) \rangle_q$  and  $\lambda_{q,n}$  in equation (19) before the fits. For all filters I used the same photonic throughput file produced for the EAZY code (Brammer et al. 2008) and kindly made available online<sup>11</sup>.

The spectroscopy was observed within slits of 1'', while the photometric observations are either measured within an aperture of 2.1'' (Muzzin et al. 2013) or total magnitudes (Weaver et al. 2022). This implies that one cannot expect a matching of the flux levels without calibration. One should also keep in mind that in some cases, with a non-uniform stellar population, the photometric fluxes may correspond to a significantly different population that that sampled by the spectra. With this caveat in mind, for every galaxy, before the PPXF fit, I computed synthetic photometric fluxes  $\langle f_\lambda \rangle_q$  from the

<sup>11</sup> Available from <https://github.com/gbrammer/eazy-photoz>

VIMOS spectra using [equation \(15\)](#), for the subset of photometric bands contained within the VIMOS wavelength range. Then I multiplied the spectrum by a factor  $\kappa$  to match it to the photometry in a least-squares sense. The factor  $\kappa$  can be computed with the general linear-fitting relation (e.g. [Cappellari 2008](#), eq. 51)

$$\kappa = \frac{\mathbf{d} \cdot \mathbf{m}}{\mathbf{m} \cdot \mathbf{m}}, \quad (24)$$

where the “data” vector  $\mathbf{d}$  has elements  $d_q = p_q/\Delta p_q$ , the observed photometric fluxes  $p_q$ , divided by their uncertainties  $\Delta p_q$  and the “model” vector  $\mathbf{m}$  has elements  $m_q = \langle f_\lambda \rangle_q / \Delta p_q$ , the synthetic fluxes also divided by the data uncertainties.

Similarly to [Kriek & Conroy \(2013\)](#), in all my fits I did not use the formal photometric uncertainties provided by the catalogues, as this would make the fits completely dominated by the very small error bars at longer wavelengths. Moreover, after performing numerous fits, it became clear that uncertainties are dominated by systematic imperfections in the SSP models assumptions or in the data, rather than by purely random noise. For this reason, I adopted for all the photometric uncertainty a constant value per galaxy (in a linear, not relative sense).

## 5.5 Outliers removal

Following common practice (e.g. [Westfall et al. 2019](#)), I remove outliers from the spectra fits by performing a first PPXF fit using the formal uncertainties, for both photometry and spectroscopy. Then I estimate the rms noise spectrum  $\sigma_{\text{noise}}^{\text{spec}}$  per pixel from the fit residuals, in a statistically robust way, by computing for every spectral pixel the interval containing 68% of the residuals, within a moving window of 100 pixels. Then I mask the pixels deviating more than  $3\sigma_{\text{noise}}^{\text{spec}}$  from the best fit. I repeat the masking in a loop, while iteratively adjusting the normalization of the best fitting spectrum using the non-masked pixels with [equation \(24\)](#), until the mask does not change anymore.

After clipping the spectroscopic outliers, I multiply  $\sigma_{\text{noise}}^{\text{spec}}$  of every pixel by  $k = (\chi^2/N_{\text{pix}}^{\text{spec}})^{1/2}$ , where  $N_{\text{pix}}^{\text{spec}}$  is the number of non-masked spectral pixels, in such a way that the resulting  $\chi^2/N_{\text{pix}}^{\text{spec}} = 1$ . I do the same rescaling for the photometric uncertainties to obtain  $\chi^2/N_{\text{pix}}^{\text{phot}} = 1$ . After the spectral masking and the rescaling of the uncertainties, I perform a second PPXF fit, from which I extract the final results.

## 5.6 Gas model and kinematic constraints

Gas emission could be predicted based on the galaxy SFH and could be included in the models, with some extra assumptions, based on photoionization models like CLOUDY ([Ferland et al. 1998, 2013](#)). This feature is implemented in `fsps` and can be useful when fitting photometry alone. However, in my case, I have many good quality spectra in addition to photometry and I want to be able to fit the gas more accurately than a model could predict. For this reason, I fit the gas emission lines in a model-independent way with PPXF.

With PPXF one can fit many gas emission lines simultaneously to the stellar continuum. This is especially important when studying the stellar population of star-forming galaxies or AGNs, where key absorption lines like the Balmer series are filled by emission. However, when fitting gas lines in relatively low S/N spectra, it is essential to set constraints on the parameters of the gas lines, to prevent possible degenerate situations. An example of a situation to avoid is when the spectrum does not have gas emission and the Gaussian describing an emission line becomes so wide as to become degenerate with the shape of the stellar continuum.

This is one of the types of situations for which I designed the linearly constrained algorithm of [Section 3.2](#). For my fits to the LEGA-C spectra, after some experimentation focusing on the few problematic fits, I found it sufficient to require the dispersion of the gas emission lines to be smaller than the stellar one  $\sigma_{\text{gas}} < \sigma_*$  and in addition I required the gas and mean stellar velocities to satisfy  $|V_{\text{gas}} - V_*| < 500 \text{ km s}^{-1}$ . I enforced these requirements as linear constraints in PPXF (keyword `constr.kinem`).

The emission lines that I included in the PPXF fits are all the lines listed in [Belfiore et al. \(2019, table 1\)](#). In particular, those falling within the LEGA-C wavelength range for  $0.6 < z < 1$  are the Balmer series bluer than  $\text{H}\beta$ , the  $[\text{OII}]\lambda\lambda 3726, 29$ ,  $[\text{NeIII}]\lambda\lambda 3868, 69$  and  $[\text{OIII}]\lambda\lambda 4959, 5007$  doublets, and the  $\text{HeII}\lambda 4687$ . I force the kinematics of all the gas lines to be the same and I additional fix the  $[\text{OIII}]$  doublet to the  $1/3$  ratio. I fit the Balmer series as single gas template with decrement for Case B recombination, for temperature  $T = 10^4 \text{ K}$  and electron density  $n_e = 100 \text{ cm}^{-3}$  from [Storey & Hummer \(1995\)](#). I allow the gas templates to have their own [Calzetti et al. \(2000\)](#) attenuation curve. Fixing the intrinsic ratios of the Balmer series allows me to provide a better extrapolation of the gas filling the weakest (higher-order) absorption lines of the series, even when the S/N of the spectrum is not high enough to constrain them.

Note that, although I do not include theoretical gas emission predictions in the SPS models, I do include the contribution of the emission lines that are spectroscopically constrained in the photometry. In particular, when Balmer lines are present in the spectrum, the line fluxes of the Balmer series, and in particular of  $\text{H}\alpha$ , which is outside the LEGA-C wavelength range, are included in the photometric fit. However, I checked that this inclusion has a minimal effect on the final results.

## 5.7 Velocity dispersion matching

The LEGA-C data have an instrumental dispersion of  $\sigma_{\text{inst}} \approx 36 \text{ km s}^{-1}$  ([Section 4.1](#)), ignoring possible variations within the rather small wavelength range. The MILES stellar templates used in both the `fsps` and `GALAXEV` models were observed with an instrumental resolution of  $\Delta\lambda \approx 2.50 \text{ \AA}$  FWHM ([Falcón-Barroso et al. 2011](#)), equivalent to  $R = \lambda/\Delta\lambda \approx 1600$  at the typical wavelength  $\lambda \approx 0.4 \mu\text{m}$  covered by LEGA-C. This corresponds to an instrumental dispersion

$$\sigma_{\text{inst}} = \frac{c}{R \sqrt{4 \ln 4}} \approx 80 \text{ km s}^{-1}. \quad (25)$$

Ideally, I would like to use SPS models based on stars with higher resolution than the galaxy spectra. However, assuming that the instrumental line spread functions are approximately Gaussian, one can still use a template with higher instrumental dispersion  $\sigma_{\text{inst,tem}}$  than that  $\sigma_{\text{inst,gal}}$  of the observed galaxy spectrum as long as  $(\sigma_{\text{inst,gal}}^2 + \sigma_*^2) > \sigma_{\text{inst,tem}}^2$ , where  $\sigma_*$  is the real “astrophysical” dispersion of the galaxy stars. After the PPXF fit one can compute the corrected stellar dispersion with the standard expressions ([Cappellari 2017](#), sec. 2.2)

$$\sigma_{\text{diff}}^2 = \sigma_{\text{inst,gal}}^2 - \sigma_{\text{inst,tem}}^2 \quad (26a)$$

$$\sigma_*^2 = \sigma_{\text{PPXF}}^2 - \sigma_{\text{diff}}^2. \quad (26b)$$

As  $\sigma_{\text{diff}}^2$  is in this case a negative quantity, I can model the dispersion of galaxies down to  $\sigma_* \gtrsim |\sigma_{\text{diff}}^2|^{1/2} = 71 \text{ km s}^{-1}$ . I compared my fitted dispersions  $\sigma_*$  with the values in the LEGA-C DR3 catalogue, which were measured with PPXF using higher resolution synthetic templates as described in [Bezanson et al. \(2018\)](#). I found a good agreement assuming  $|\sigma_{\text{diff}}^2|^{1/2} \approx 48 \text{ km s}^{-1}$ , which suggests possible inaccuracies

in the quoted relative instrumental dispersion of the galaxies and the templates. Regardless of the reason for this discrepancy, only 40 of the 3197 galaxies in the catalogue with measured dispersion have  $\sigma_* < 48 \text{ km s}^{-1}$ , likely due to measurement uncertainties. This implies that I can safely use the SPS based on MILES models to study the stellar population of LEGA-C galaxies.

## 6 RESULTS

### 6.1 Spectral fit examples

In this paper, I focus on galaxy observable trends rather than on comparisons with models of galaxy formation. For this reason, instead of converting the SFH recovered by ppxf into stellar masses formed in a given time interval, I will always show the fraction of bolometric luminosity contributed by each template, as a function of their age and metallicity  $[M/H]$ . More precisely, I integrate the luminosity from the template spectra only within the region  $0.1 < \lambda < 3 \mu\text{m}$  covered by the data. This is to avoid the possibility of interpreting very young stars, which emit most of their luminosity for  $\lambda < 0.1 \mu\text{m}$ , as contributing significantly to my observables, even when their flux is not detected in the data, but simply extrapolated. I still indicate my luminosity as  $L_{\text{bol}}$  because, except for extreme young stars, it still represents a very good approximation for it.

The advantage of using  $L_{\text{bol}}$  rather than SFH, is that one can get a direct sense of what the data actually show, without strongly non-linear conversions into masses, due to the large  $M/L$  differences of different stellar populations. In fact, I would argue that comparisons with models of galaxy formations are generally more meaningful when the models, for which all quantities are known accurately, are converted into luminous observables, rather than trying to do the reverse by extracting SFH in masses from the data.

In the course of this study, I fitted the 3197 galaxies of my sub-sample (Section 4.1) with ppxf multiple times with different levels of regularization, or no regularization at all, to test the sensitivity of the results. In Fig. 3 I illustrate the effect of regularization on some high- $S/N$  spectra. These figures, like Fig. 1, illustrate the ill-conditioning of the stellar population inversion, which prevents one from obtaining a unique solution, even from very good data. Nonetheless, the figure also illustrates the ability of the method to distinguish the striking difference between (i) galaxies that can only be described, even at high regularization<sup>12</sup> (regul=100) by a single star formation event at a very localized lg Age (top three panels in Fig. 3) and (ii) galaxies that require multiple and separated star formation events to be described (bottom three panels in Fig. 3). The galaxies in the top panels are essentially described by a single SPS model, from  $0.1 \mu\text{m}$  to  $3 \mu\text{m}$ , for both spectra and photometry. This highlights the success of the SPS models in accurately predicting real galaxy spectra.

In Fig. 4 I show additional examples of ppxf fits to good quality spectra to give a sense of the variety of spectral morphologies and the corresponding variations in the  $L_{\text{bol}}$  weights distributions. I used in all these cases a high regularization (regul=100). Also here one can clearly see the striking difference between (i) the three galaxies in the top row, which can only be described as a single burst

<sup>12</sup> A given value of the ppxf keyword regul roughly implies that neighbouring weights  $w_{ij}$  can differ by  $\Delta w_{ij} \sim 1/\text{regul}$ . As I normalize all galaxy spectra to the same average flux (e.g. average=1), setting a given regul value roughly corresponds to requiring a similar level of smoothness in the weights distribution.

of star formation, which happened at different times and (ii) galaxies requiring multiple discrete star formation events. Star formation events appear to have a similar extent in ln Age, which seems to imply that events in the past lasted longer than recent ones. This is likely an artefact of our general ability to more accurately detect age differences in recent events.

### 6.2 Stellar population scaling relations

As I am focusing on observable trends, I define luminosity-weighted population quantities, summed over the template weights, as

$$\langle \lg \text{Age} \rangle = \frac{\sum_j L_{\text{bol},j} \times \lg \text{Age}}{\sum_j L_{\text{bol},j}} \quad (27a)$$

$$\langle [M/H] \rangle = \frac{\sum_j L_{\text{bol},j} \times [M/H]}{\sum_j L_{\text{bol},j}}. \quad (27b)$$

In Fig. 5 I show the distribution of ages, metallicities and the Sersic (1968) exponent  $n_{\text{Ser}}$  on the  $(M_*, R_e^{\text{maj}})$  plane. Here I adopted as an approximation of the total stellar masses  $M_*$  the virial mass  $M_{\text{vir}} \propto R_e^{\text{maj}} \sigma_*^2$ , and as half-light radius  $R_e^{\text{maj}}$  the semi-major axis of the isophote containing half of the total light of the Sersic (1968) fitted to the galaxy photometry. Both quantities, as well as  $n_{\text{Ser}}$  are tabulated in the LEGA-C catalogue (van der Wel et al. 2021). See Cappellari et al. (2013a) for a discussion of why the virial mass is likely to be a better approximation of the total stellar mass than the corresponding stellar population estimate. I LOESS smoothed the the measured values using the algorithm by Cleveland & Devlin (1988) as implemented<sup>13</sup> by Cappellari et al. (2013b). I used a small smoothing parameter `frac=0.1` in all plots of this paper.

This figure shows the well-known fact, in the nearby Universe, that both ages and metallicities approximately follow lines of constant stellar velocity dispersion  $\sigma_*$ , or equivalently lines where  $M_* \propto R_e^{\text{maj}}$  (compare this figure with fig. 4 of Li et al. 2018). I also show to guide the eye the local ‘‘zone of avoidance’’ at high densities (Cappellari et al. 2013b, eq. 4), which I scaled down by a factor  $1.6 \times$  in  $R_e^{\text{maj}}$ , roughly consistent with the general trends of decreasing galaxy sizes with redshift (e.g. van der Wel et al. 2014). The Sersic index  $n_{\text{Ser}}$  also approximately follows the distribution of ages and metallicity, in the sense that passive galaxies tend to have  $\ln n_{\text{Ser}} \gtrsim 0.4$  or  $n_{\text{Ser}} \gtrsim 2.5$  (red colour in the right panel of Fig. 5). This  $n_{\text{Ser}}$  value is the one sometimes adopted to separate early-type from late-type galaxies (e.g. Bell et al. 2003; Shen et al. 2003). In the local Universe, below the stellar mass  $\lg(M_*/M_\odot) \lesssim 11.5$  the trend of  $n_{\text{Ser}}$  is due to a sequence of increasing bulge fraction, while above  $\lg(M_*/M_\odot) \gtrsim 11.5$  is the region of slow rotators with cores (see review by Cappellari 2016, fig. 23).

This result has a rather long history, both locally and at  $z \sim 1$  (Chauke et al. 2018, 2019; Beverage et al. 2021; Barone et al. 2022; Hamadouche et al. 2022; Tacchella et al. 2022) but had not been seen so cleanly at this redshift before LEGA-C. For nearby galaxies, Kauffmann et al. (2003) clearly noted that galaxy population correlates better with mass surface density  $\Sigma$  than with  $M_*$ . It was later observed that  $\Sigma$ , or even better the virial predictor  $\sigma_{\text{vir}} \propto M_*/R_e$  of the stellar velocity dispersion, inferred from photometry alone, remains a better predictor of galaxy colours out to  $z \approx 3$  (Franx et al. 2008; Bell et al. 2012). However, it was still unclear at that time how accurately the photometric estimates were able to predict the actual stellar masses and the velocity dispersion of the stars. To address this issue I used high-quality dynamical models, and real good quality

<sup>13</sup> Available from <https://pypi.org/project/loess/>

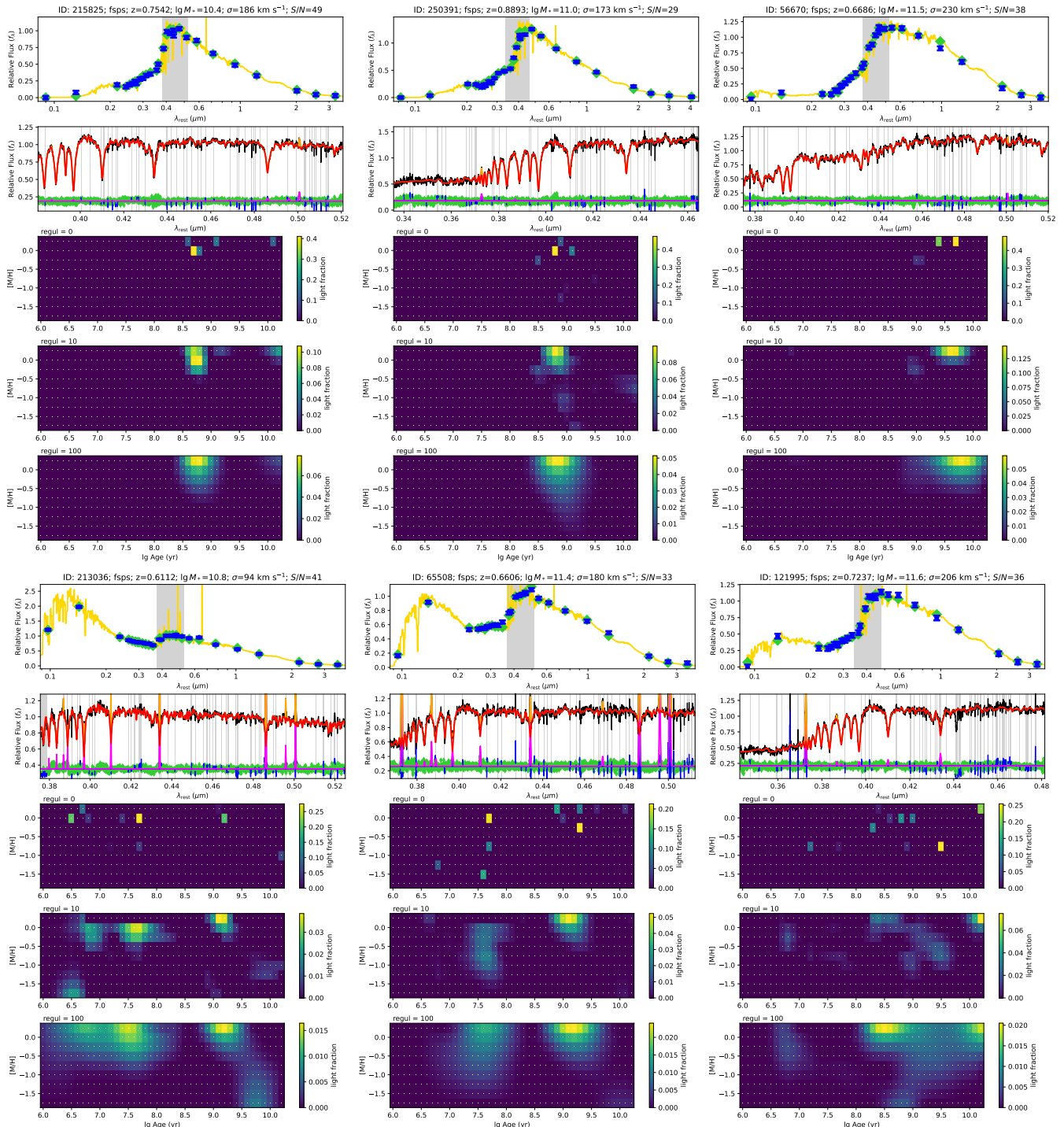


**Figure 3.** Examples of PPXF fits to the LEGA-C galaxy spectra and 28-bands photometry using the `fsps` models. The top three galaxies require a model with a single short star formation event, while the bottom three galaxies require multiple discrete star formation events. For each galaxy, the top panel shows the photometric measurements (blue error bars) and the best fit (green diamonds), while the golden line shows the underlying best fitting template with included emission lines. The grey vertical band indicates the range where spectroscopy was also fitted. The second panel shows the observed spectrum (black line) and the best fitting total spectrum (orange line). The best fitting stellar spectrum alone is shown in red and the gas emission one is in magenta. The residuals (arbitrarily offset) are indicated with green diamonds and the masked pixels with blue lines (and corresponding grey vertical bands). The last three panels show the distribution of the PPXF weights, indicating the bolometric luminosity  $L_{\text{bol}}$  of each stellar population of given age and metallicity. The weights are shown for (i) no regularization, (ii) regularization  $\text{regul}=10$  and (iii)  $\text{regul}=100$  as written in the plots.

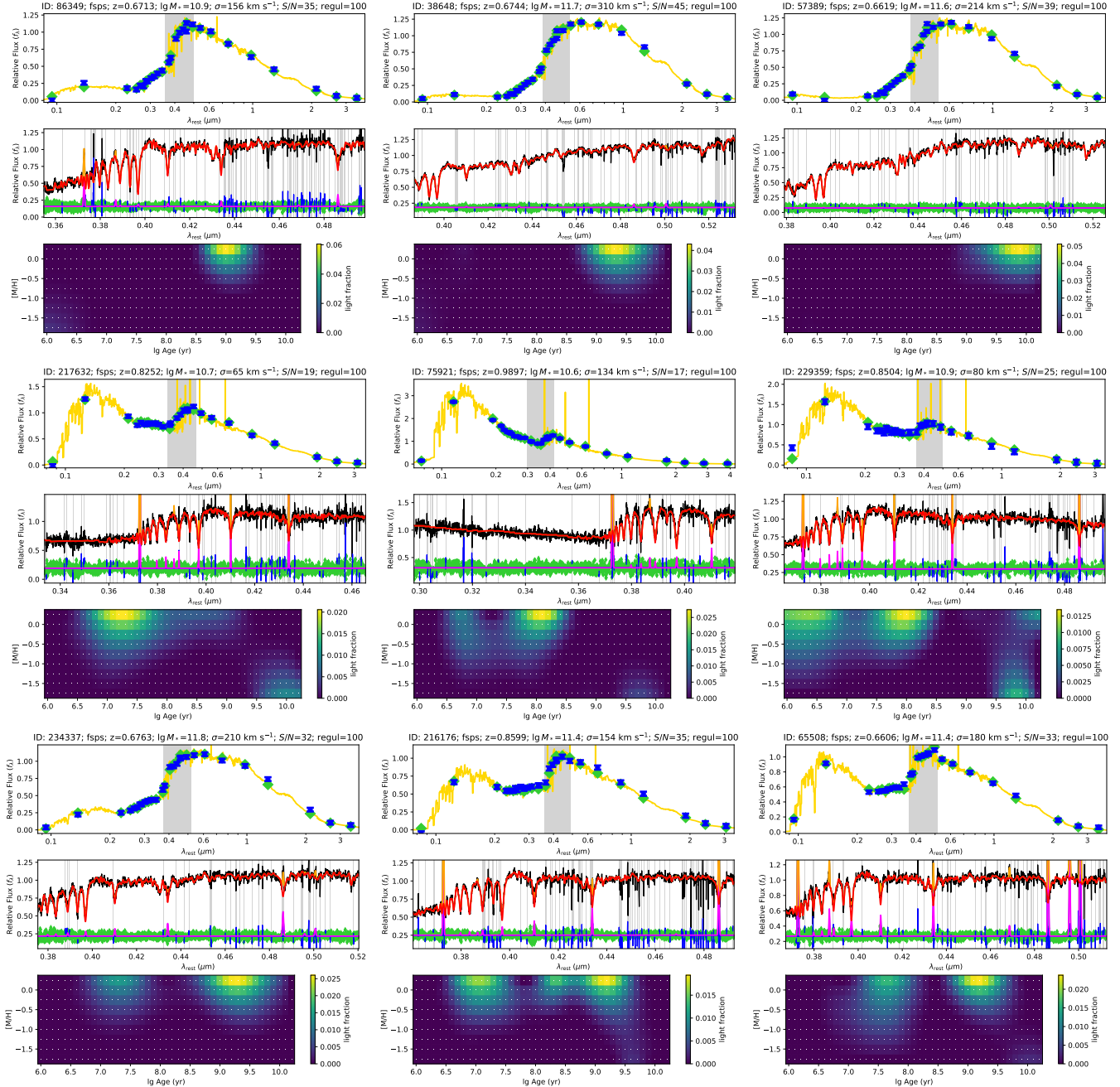


**Figure 4.** More examples of ppxf fits to spectra and photometry. The meaning of the symbols is the same as in Fig. 3, but I show a single regularization (regul=100). The top three galaxies require a single star formation event, while the rest can only be modelled with multiple discrete star formation events.

stellar kinematics and dynamically determined masses, rather than photometric estimates. In Cappellari (2011) I clearly concluded that “ $\sigma_*$  (not  $\Sigma$  or  $M_*$ ) is the best predictor of galaxy properties” (see also Cappellari et al. 2013b). These early results were confirmed by several papers using larger samples and stellar kinematics of ever-increasing quality (e.g. Wake et al. 2012; Scott et al. 2017; Li et al. 2018; Barone et al. 2018, 2020). In parallel, Cheung et al. (2012) and Fang et al. (2013) introduced the use of central surface density from photometry, within a fixed radius of 1 kpc, to predict quenching. A review is given in Cappellari (2016, see fig. 22).

Given that in Fig. 5 the main stellar population trends follow  $\sigma_*$ , in Fig. 6 I show how the luminosity-weighted ages and metallicity

depends on  $\sigma_*$  in the LEGA-C sample. The trends resemble quite closely the local results from the best integral-field spectroscopy from both SAMI (Scott et al. 2017) and MaNGA (Li et al. 2018). However, the top panels of Fig. 6 additionally illustrate the clear dependency between age and  $[M/H]$  at fixed  $\sigma_*$ : the population of old galaxies at large  $\sigma_*$  is characterized by a larger metallicity than their younger counterpart at the same  $\sigma_*$ . Very clear is the bend in the  $(\sigma_*, \text{Age})$  distribution around  $\lg(\sigma_*/\text{km s}^{-1}) \approx 2.3$  (also see Chauke et al. 2018). The results are very consistent between both the fsps and GALAXEV SPS models. It is reassuring to see that the ridge of the age distribution in the top panels converges towards the age of the Universe at that redshift (grey horizontal band), while being slightly

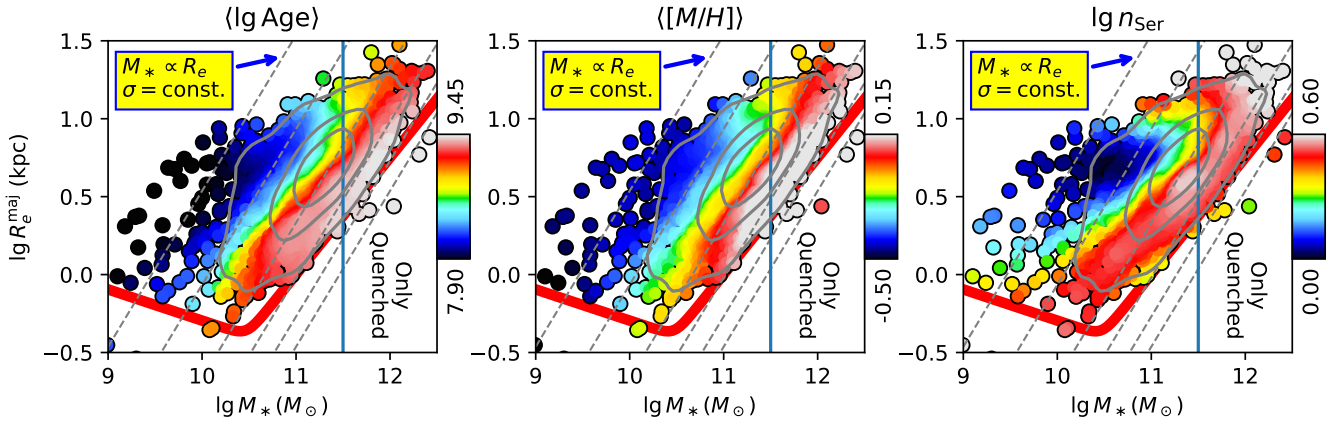


**Figure 5.** Galaxy properties on the stellar mass vs size ( $M_*$ ,  $R_e^{\text{maj}}$ ) plane at  $z \approx 0.8$ . Galaxies are coloured by their luminosity-weighted ages ( $\text{lg Age}$ ) (left panel), luminosity-weighted metallicities ( $\langle [M/H] \rangle$ ) (middle panel) and by the Sersic index  $n_{\text{Ser}}$  of a fit to their photometry. I used the values from the GALAXEV models, but those from fSPS are very similar. All values are LOESS smoothed to show average trends and I used  $\text{regul}=10$  in ppxf. The grey contours are a kernel density estimate of the galaxy distribution (using `scipy.stats.gaussian_kde`). Galaxy properties mainly follow lines of constant stellar velocity dispersion, which is indicated by the dashed grey lines for  $\sigma_* = 50, 100, 200, 300, 400, 500 \text{ km s}^{-1}$  from left to right, while mass is not a good predictor of their stellar population. However, above a stellar mass  $\text{lg}(M_*/M_\odot) \gtrsim 11.5$  (blue vertical line), all galaxies are old (quenched), have a high metallicity and large Sersic index. The thick red line is the “zone of avoidance” for nearby galaxies from Cappellari et al. (2013b), scaled down by a factor  $1.6 \times$  to account for redshift evolution.

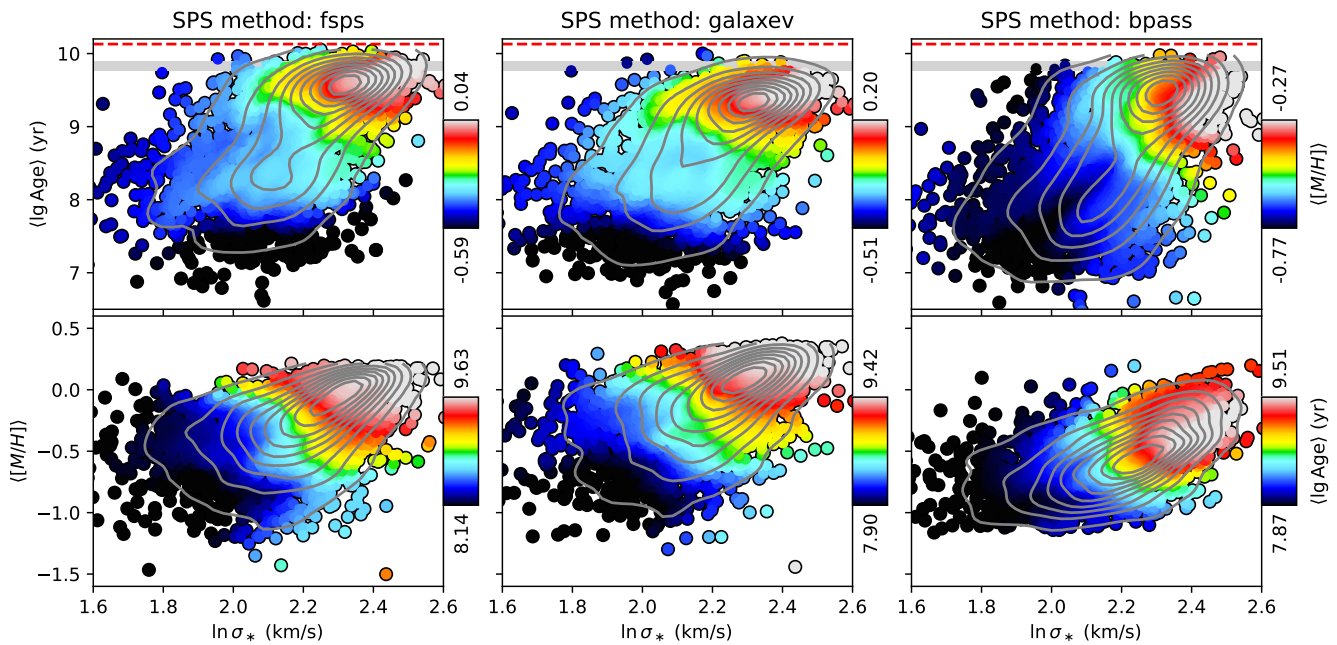


**Figure 6.** Luminosity-weighted ages ( $\text{lg Age}$ ) and metallicities ( $\langle [M/H] \rangle$ ) vs stellar velocity dispersion  $\sigma_*$  for the LEGA-C galaxies. The top panels show the age distribution, coloured by metallicity. The bottom panels show the metallicity distribution coloured by age. In all panels, the grey contours are the kernel density estimator of the galaxies’ distribution. From left to right I show results using the fSPS, GALAXEV and BPASS SPS models, all with  $\text{regul}=10$  in ppxf. There is a clear bend of the ( $\text{Age}_e, \sigma_*$ ) trend around  $\text{lg}(\sigma_*/\text{km s}^{-1}) \approx 2.3$ . At fixed  $\sigma_*$  metallicity depends on age with younger galaxies having lower  $\langle [M/H] \rangle$ .

younger for GALAXEV vs fSPS. The BPASS results are qualitatively in agreement but show substantial quantitative differences, especially in the  $\sigma_* - [M/H]$  trend. Overall, this figure confirms the quality and consistency of these global results compared to local surveys.

Fig. 7 shows the distribution of the two dust attenuation parameters  $A_V$  and  $\delta$  coloured by mean stellar age (Section 5.3). One can see that at every UV slope  $\delta$  the youngest galaxies have the strongest at-

tenuation, except for the largest  $\delta$ . Moreover, the largest attenuations in galaxies are only observed at large  $\delta$ , close to the Calzetti et al. (2000) slope  $\delta = 0$ . Note, however, that there is a degeneracy between attenuation and continuum normalization near the upper limit of  $\delta$ . Results are extremely consistent for the fSPS and GALAXEV SPS models, but again the BPASS results look quite different, although they all qualitatively agree.

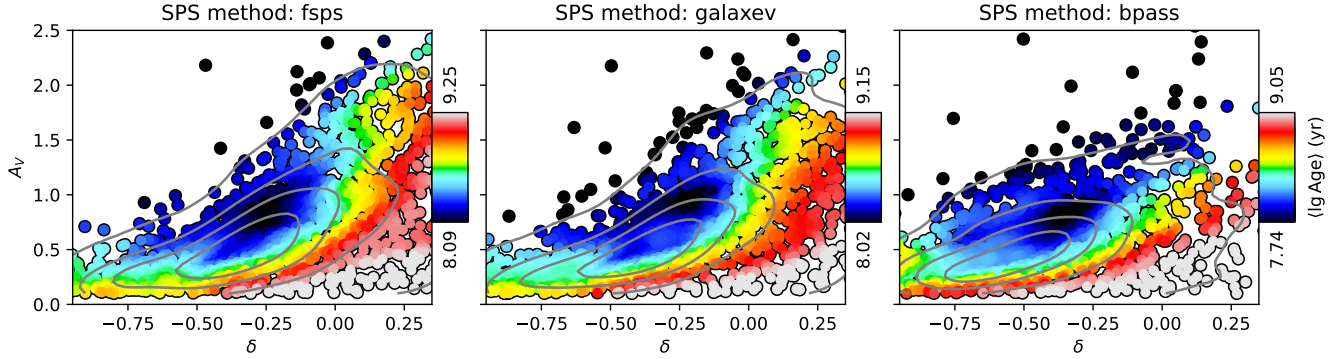


**Figure 7.** Dust properties vs galaxy age. The  $V$  band attenuation  $A_V$  in mag is plotted against the UV slope  $\delta$ . At every  $\delta$  the youngest galaxies have larger attenuation, while the largest  $A_V$  are only observed around the Calzetti et al. (2000) attenuation curve, which has  $\delta = 0$ . From left to right I show results using the fssp, GALAXEV and BPASS SPS models. The first two are highly consistent, but the latter, while still qualitatively similar is quantitatively very different.

### 6.3 Non-parametric star formation histories

Fig. 8 shows the non-parametric star formation history of the galaxies in the LEGA-C sample as a function of key galaxy parameters. For this plot I sorted the quantity of interest (e.g.  $\sigma_*$ ) and constructed 30 bins in that quantity, each containing the same number of about 100 galaxies, in such a way that different bins have the same level of shot noise. I show the dependency of the SFH, parametrized as discussed by the light  $L_{\text{bol}}$  contributed in the spectrum by stellar populations of different ages, as a function of the following parameters:

(i) **Stellar velocity dispersion:** the plots show a clear trend of SFH with  $\sigma_*$  as expected from the trends between  $\sigma_*$  and age. What is new is the striking sharpness of the boundary between a regime  $\lg(\sigma_*/\text{km s}^{-1}) \gtrsim 2.3$  (or  $\sigma_* \gtrsim 200 \text{ km s}^{-1}$ ), above which the spectra are dominated by a population nearly as old as the Universe at that redshift, without evidence for subsequent star formation events, and below which suddenly galaxies have star formation at any time until the present time. Both the fssp and GALAXEV SPS models indicate that galaxies still form the bulk of their stars at old times, but this age increases with  $\sigma_*$  by roughly a factor between 6–10 for a variation in  $\sigma_*$  by a factor of 10. In the case of the GALAXEV models, the SFH indicate ongoing star formation at the lowest  $\sigma_*$  bins, while this is less so for the fssp models.

(ii) **Galaxy mass:** contrary to the dependency of SFH with  $\sigma_*$ , the trend is more gradual as a function of stellar mass. Only galaxies more massive than  $\lg(M_*/M_\odot) \gtrsim 11.5$  are characterized by a single event of star formation at old times.

(iii) **Galaxy metallicity:** this panel shows that  $[M/H]$  is as good as  $\sigma_*$  at predicting the boundary between the region of fully quenched galaxies and those that can have multiple star formation events. Here it happens at  $[M/H] \approx -0.2$  for the fssp and  $[M/H] \approx 0.0$  for the GALAXEV, which are systematically shifted to larger values of metallicity.

(iv) **Sersic index:** This panel show the SFH as a function of the Sersic (1968) exponent  $n_{\text{Ser}}$ . The boundary between fully quenched galaxies and galaxies that can have multiple star formation events happens here at  $\lg n_{\text{Ser}} \approx 0.5$  or  $n_{\text{Ser}} \approx 3.2$ . Remarkably this boundary is here nearly as clean as that with  $\sigma_*$ .

In all panels, the results using the BPASS SPS models are again quite different from the other two. They show significant structure at specific ages and a less clear quenching boundary. The structure seen using the BPASS models is likely an artefact of the SPS rather than a real conspiracy in the star formation events.

The trends for different galaxy parameters, and the overall consistency between the four panels, for both the fssp and GALAXEV SPS models, can be understood by looking at Fig. 5 and noting that there is a region  $\lg(M_*/M_\odot) \gtrsim 11.5$  above which all galaxies are quenched, high metallicity and have large Sersic index. Below that mass galaxies follow a trend of increasing bulge fraction, which increases  $\sigma_*$ , metallicity and makes galaxies more likely to quench. These results parallel those which have been extensively reported for local galaxies (see review by Cappellari 2016). What is new here is the clarity and sharpness of the empirical evidence of the boundary to quenching and the fact that this can be detected so well at a time when the Universe was half of its current age.

A rapid cessation of star formation for galaxies above a given critical value of  $\sigma_*$ , or of some other estimate of the central stellar density, varying with  $z$ , has often been invoked to explain the evolution of galaxy parameters over time (e.g. van Dokkum et al. 2015). An excellent review of the empirical evidence and models of a quenching boundary in galaxies is given in Chen et al. (2020, sec. 1). The physical mechanism for quenching is still under debate. Very briefly, one can group the main proposed theories into three broad classes: (i) “halo quenching”, where the gas gets shock-heated when falling into the gravitational potential of massive dark halos (e.g. Dekel & Birnboim 2006); (ii) “active galactic nucleus (AGN) feedback”, where a jet from the supermassive black hole either ejects the gas from its host galaxy (e.g. Silk & Rees 1998) or prevent it from infalling (e.g. Bower et al. 2006; Croton et al. 2006). See review by Somerville & Davé (2015). The panels in Fig. 8 provide a beautiful empirical confirmation of the theoretical assumptions that are made in many of those models.

### 6.4 Non-parametric joint SFH and metallicity distributions

Fig. 9 presents the non-parametric joint luminosity distribution of the age and metallicities of the stellar populations of galaxies in four different bins of  $\sigma_*$ . As in Fig. 8, also for this figure I sorted galaxies as a function of their  $\sigma_*$  and constructed four groups, of about 800 galaxies each, to ensure all panels have the same level of shot noise. Like before, I compare all three SPS models (fssp, GALAXEV and BPASS). In addition, In the second row of Fig. 9 I show the result when using the fssp model but adopting the photometric measurements from COSMOS 2020 (Weaver et al. 2022) instead of the UltraVista catalogue (Muzzin et al. 2013). The first and second rows are barely distinguishable and this shows that any possible differ-

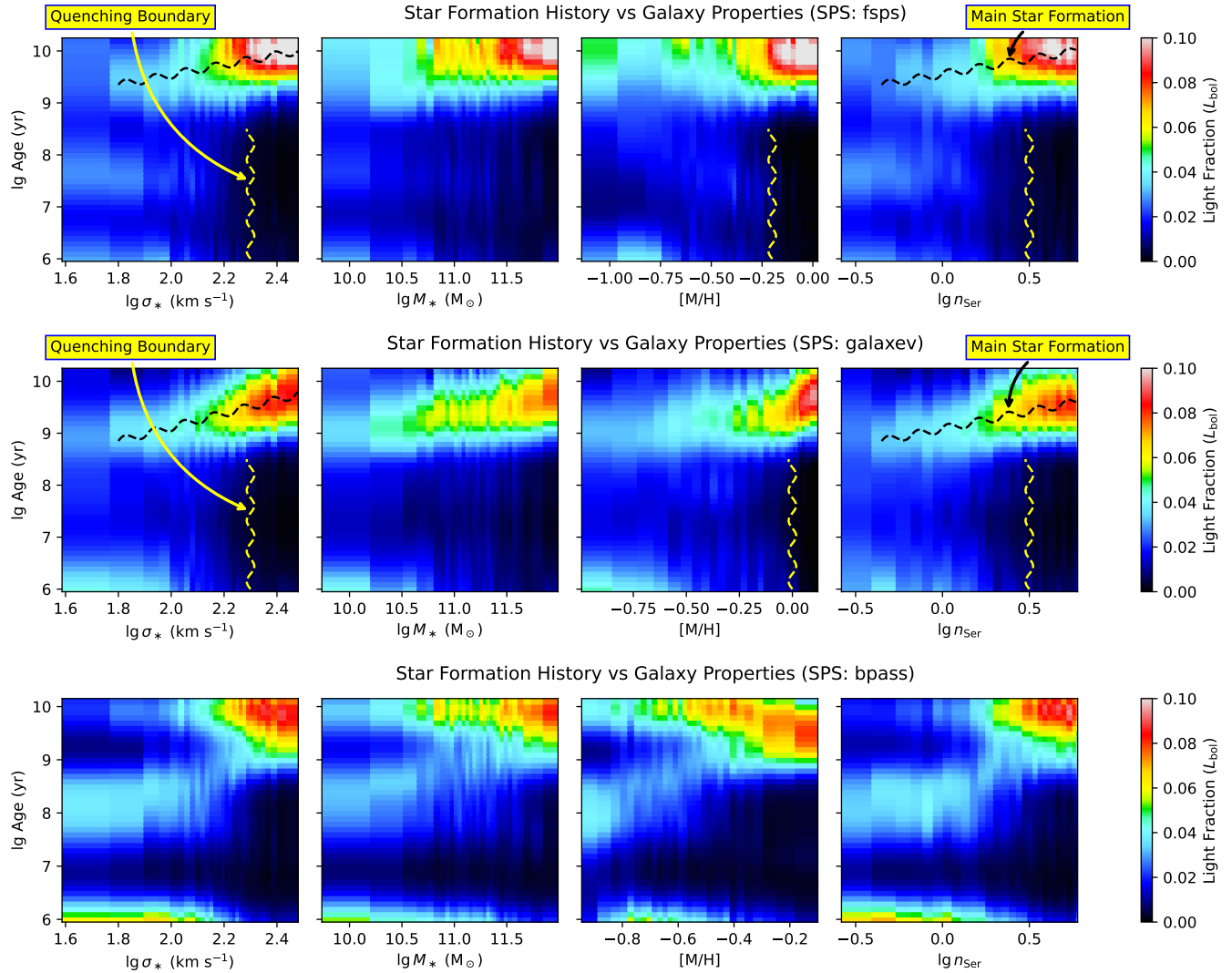


**Figure 8.** Star formation history (SFH) vs galaxy properties. In all panels, the colours represent the SFH recovered with `ppxf` (with `regul=100`) parametrized by the bolometric light  $L_{\text{bol}}$  fraction contributed by populations of different ages. The SFHs are shown as a function of key galaxy parameters: the stellar velocity dispersion  $\sigma_*$ , the stellar mass  $M_*$ , the luminosity weighted metallicity  $\langle [M/H] \rangle$  and the exponent  $n_{\text{Ser}}$  of a Sersic profile fitted to the galaxy photometry (see text for definitions). Average values are computed for equal bins in  $\sigma_*$  (or the other parameters) of 100 galaxies each. Galaxies with largest  $\sigma_*$ ,  $M_*$ ,  $\langle [M/H] \rangle$  or  $n_{\text{Ser}}$  on average experienced their main star formation event long ago, but the typical age for the bulk of their star formation increases with  $\sigma_*$  (or the other parameters) as indicated by the slanted black dashed wavy lines in the left and right panels. For lower  $\sigma_*$  galaxies can form the stars at any time until the present. The plots show a beautifully clear and sharp quenching boundary at  $\lg(\sigma_*/\text{km s}^{-1}) \approx 2.3$ , or  $\langle [M/H] \rangle \approx -0.2$  for fspS and  $\langle [M/H] \rangle \approx 0$  for GALAXEV, or  $\lg n_{\text{Ser}} \approx 0.5$ , as indicated by the vertical yellow dashed wavy lines. The boundary is more gradual as a function of mass and roughly happens around  $\lg(M_*/M_\odot) \approx 11.5$ . Note the generally good agreement between the results from the fspS and GALAXEV SPS. The results using the BPASS models look problematic, with spurious structures at specific ages, which are most likely artefacts of the models.

ence in the photometric calibration has a completely insignificant effect on the results. The distribution from both fspS and GALAXEV is highly consistent, almost at the level of the individual ‘blobs’, with the exception of slightly older younger ages and higher metallicities for the GALAXEV vs the fspS models.

The plots indicate that even galaxies with low  $\sigma_*$  are still dominated by stars with high metallicity, but this is diluted by extra lower-metallicity populations acquired at different times. I should stress that the relatively smooth distribution in the maps are averages of many galaxies and should not be interpreted as the evolution of one individual galaxy, which is generally characterized by discrete star formation events.

As expected, the BPASS models show again quite different results, with a markedly different metallicity distribution. As commented earlier, the results from this model should be treated with caution as they are likely dominated by spurious unknown effects in the models.

A caveat on these results on the metallicity distribution, which also affects other similar results on metallicity determinations from galaxy stellar spectra, is that the signature of metallicity variations becomes weaker at younger ages, where the  $S/N$  of the data also generally decreases. This can introduce possible systematic effects on metallicity trends. To exclude the effect of  $S/N$ , I verified that all results remain unchanged if I restrict the analysis to the 873 galaxies

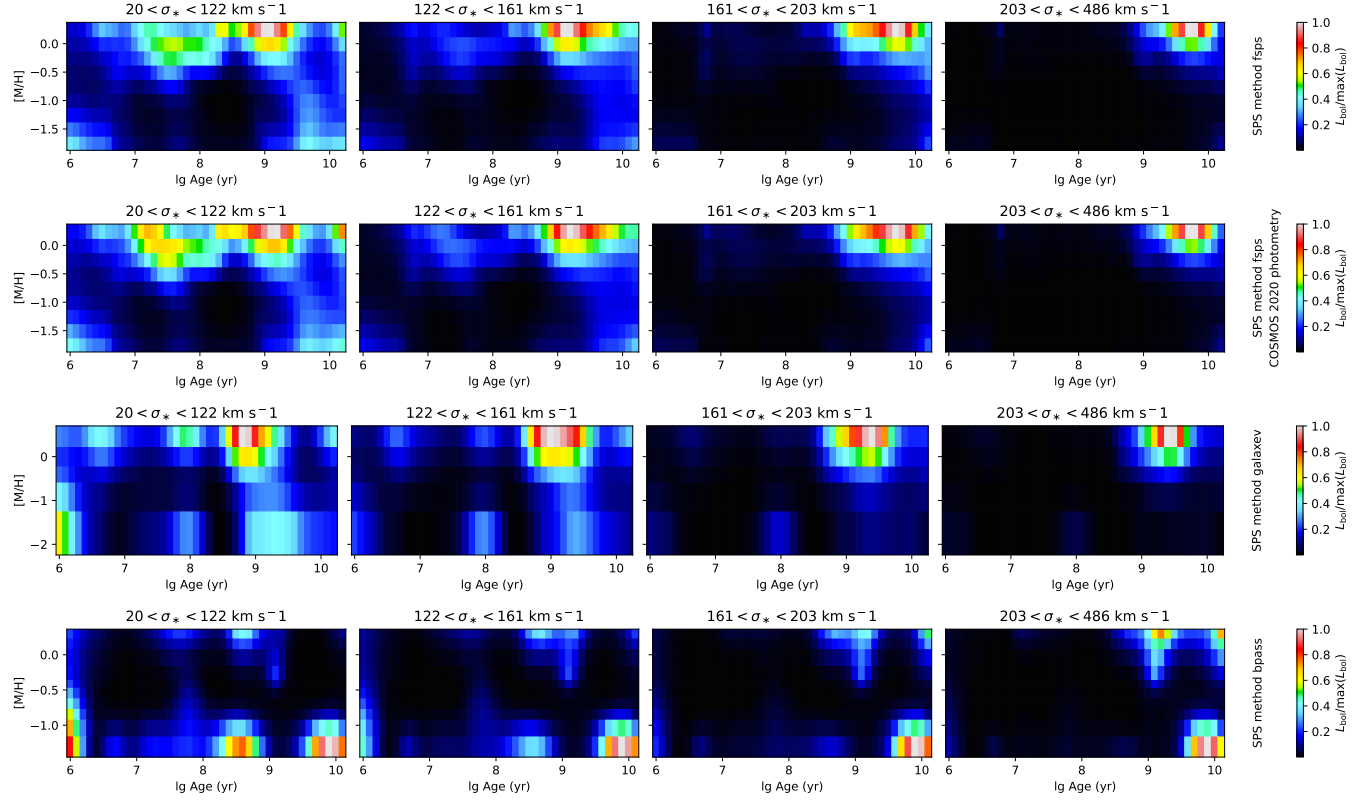


**Figure 9.** Joint star-formation history (SFH) and metallicity distributions. Each panel shows the average distribution of weights recovered with ppxf (with  $\text{regul}=10$ ) for 4 bins containing 800 LEGA-C galaxies sorted by their stellar velocity dispersion  $\sigma_*$  (as indicated in the plot titles). The weights represent the bolometric luminosity  $L_{\text{bol}}$  contributed by populations of different ages and metallicities. The top row shows the results obtained with the fSPS SPS models, the second row still uses fSPS but adopts the COSMOS 2020 (Weaver et al. 2022) instead of the UltraVista photometric catalogue (Muzzin et al. 2013). The third row is derived using the GALAXEV SPS models and the bottom one with the BPASS models. One can see that the fSPS and GALAXEV SPS provide qualitatively consistent results even for some of the main ‘‘blobs’’ in the distributions. Using an alternative photometric catalogue has virtually no effect on the results. At large  $\sigma_*$  galaxies on average quenched long ago and their stars have high metallicity. At progressively lower  $\sigma_*$  the age of the bulk of the star formation decreases, while still being dominated by high metallicity stars. However, the population is polluted by fresh accretion events of lower metallicity and a range of accretion times. As previously noted, the results using BPASS SPS models are significantly different and should not be trusted, without further analysis.

with  $S/N > 20$  and even, at coarser resolution, for the subset of 126 galaxies with  $S/N > 40$ . It would still be valuable to compare the reported metallicity trends e.g. with those inferred from gas tracers from similar data.

## 7 SUMMARY

In the first half of this paper, I described some modifications to the ppxf method (Cappellari 2017), which is used to extract the stellar and gas kinematics, as well as the stellar population of galaxies. First, I described a novel constrained least-squares optimization algorithm that ppxf has been using for the past few years. Then I outlined the changes I made to ppxf to be able to fit photometric data together with the usual full-spectrum fitting. I also described some other minor changes.

In the second half of the paper, I presented an application of ppxf to the extraction of non-parametric star formation histories and metallicity distributions for a sample of 3200 galaxies at redshift  $0.6 < z < 1$  with spectroscopy from the LEGA-C survey DR3 (van der Wel et al. 2021), and with 28-bands photometric measurements covering from the far ultraviolet ( $0.1 \mu\text{m}$ ) to the near-infrared

( $3 \mu\text{m}$ ) from either the UltraVista (Muzzin et al. 2013) or the COSMOS 2020 catalogues (Weaver et al. 2022).

For this study, I used and compared three spectral population synthesis (SPS) methods satisfying some criteria of age and wavelength coverage. This led to my selection of the fSPS (Conroy et al. 2009; Conroy & Gunn 2010), GALAXEV (Bruzual & Charlot 2003) and BPASS (Stanway & Eldridge 2018; Byrne et al. 2022) SPS methods.

I found that ppxf on these data reveals a striking difference between galaxies that are only consistent with a single star formation event from those that require multiple bursts of star formation.

I constructed scaling relations for the global stellar population parameters and found a remarkable similarity, but even clearer trends, between these results at  $z \approx 0.8$  and those from the latest spectroscopic surveys in the nearby Universe. This gives some confidence in the meaningfulness of the results and highlights the quality of the spectro-photometric data.

Finally, I explored the non-parametric star formation histories (SFH) and the joint SFH and metallicity  $[M/H]$  distributions. I found that the data indicate, on average over many galaxies, a remarkably sharp boundary for the cessation of star formation (or quenching), at a stellar velocity dispersion  $\sigma_* \approx 200 \text{ km s}^{-1}$ , or equivalently at metallicity  $[M/H] \approx -0.1$  (with some variation

dependent on the adopted SPS model) or at Sersic (1968) index  $\lg n_{\text{Sers}} \approx 0.5$ . As expected, the boundary is less sharp as a function of stellar mass. This abrupt quenching boundary has been invoked by several models of galaxy formation. These data provide one of the cleanest empirical evidence to date.

This paper only scratches the surface of what can be done with this dataset and with similar ones that are being acquired at comparable and higher redshift. I have not explored e.g. obvious dependencies between SFH and stellar kinematics or environment (Cole et al. 2020; Sobral et al. 2022, e.g.). Comparisons with galaxy formation models should be performed in the space of observable rather than using stellar masses which are empirically more uncertain. A similar analysis at higher redshift can reveal the onset and variation of the quenching boundary, which is a key but still a quite uncertain parameter in galaxy formation models. James Webb Space Telescope (JWST) data are ideal to extend this kind of study to higher redshift.

## REFERENCES

Aihara H., et al., 2019, *Publications of the Astronomical Society of Japan*, **71**

Andersen M., Dahl J., Liu Z., Vandenberghe 2011, in Lieven Sra S., Nowozin S., Wright S. J., eds., Optimization for Machine Learning. MIT Press Cambridge, MA, pp 55–83, doi:10.7551/mitpress/8996.003.0005

Andersson C. A., Bro R., 2000, *Chemometrics and Intelligent Laboratory Systems*, **52**, 1

Arnouts S., et al., 2002, *MNRAS*, **329**, 355

Baade W., 1963, Evolution of Stars and Galaxies. Harvard University Press, doi:10.4159/harvard.9780674280311

Bacon R., et al., 2010, in McLean I. S., Ramsay S. K., Takami H., eds, SPIE Conference Series Vol. 7735, Ground-based and Airborne Instrumentation for Astronomy III. p. 8, doi:10.1117/12.856027

Baldry I. K., 2018, arXiv e-prints, p. arXiv:1812.05135

Barone T. M., et al., 2018, *ApJ*, **856**, 64

Barone T. M., D’Eugenio F., Colless M., Scott N., 2020, *ApJ*, **898**, 62

Barone T. M., et al., 2022, *MNRAS*, **512**, 3828

Belfiore F., et al., 2019, *AJ*, **158**, 160

Bell E. F., McIntosh D. H., Katz N., Weinberg M. D., 2003, *ApJS*, **149**, 289

Bell E. F., et al., 2012, *ApJ*, **753**, 167

Belli S., Newman A. B., Ellis R. S., 2014, *ApJ*, **783**, 117

Belli S., Newman A. B., Ellis R. S., 2017, *ApJ*, **834**, 18

Benitez N., 2000, *ApJ*, **536**, 571

Bessell M., Murphy S., 2012, *PASP*, **124**, 140

Bevacqua D., Cappellari M., Pellegrini S., 2022, *MNRAS*, **511**, 139

Beverage A. G., Kriek M., Conroy C., Bezanson R., Franx M., van der Wel A., 2021, *ApJ*, **917**, L1

Bezanson R., et al., 2018, *ApJ*, **868**, L36

Bolzonella M., Miralles J. M., Pelló R., 2000, *A&A*, **363**, 476

Bower R. G., Benson A. J., Malbon R., Helly J. C., Frenk C. S., Baugh C. M., Cole S., Lacey C. G., 2006, *MNRAS*, **370**, 645

Brady M., Horn B. K. P., 1983, *Computer Vision, Graphics, and Image Processing*, **22**, 70

Brammer G. B., van Dokkum P. G., Coppi P., 2008, *ApJ*, **686**, 1503

Branch M. A., Coleman T. F., Li Y., 1999, *SIAM Journal on Scientific Computing*, **21**, 1

Bruzual G., Charlot S., 2003, *MNRAS*, **344**, 1000

Bryant J. J., et al., 2015, *MNRAS*, **447**, 2857

Bundy K., et al., 2015, *ApJ*, **798**, 7

Bunn E. F., Hogg D. W., 2009, *American Journal of Physics*, **77**, 688

Byrne C. M., Stanway E. R., Eldridge J. J., McSwiney L., Townsend O. T., 2022, *MNRAS*, **512**, 5329

Calzetti D., Armus L., Bohlin R. C., Kinney A. L., Koornneef J., Storchi-Bergmann T., 2000, *ApJ*, **533**, 682

Capak P., et al., 2007, *ApJS*, **172**, 99

Cappellari M., 2008, *MNRAS*, **390**, 71

Cappellari M., 2011, in Paper presented at the conference on Galaxy Formation held 18–22 July, 2011 at Durham University, Durham, UK. Online at <http://astro.dur.ac.uk/Gal2011/talks.php>.

Cappellari M., 2016, *ARA&A*, **54**, 597

Cappellari M., 2017, *MNRAS*, **466**, 798

Cappellari M., Emsellem E., 2004, *PASP*, **116**, 138

Cappellari M., et al., 2011, *MNRAS*, **413**, 813

Cappellari M., et al., 2013a, *MNRAS*, **432**, 1709

Cappellari M., et al., 2013b, *MNRAS*, **432**, 1862

Carnall A. C., McLure R. J., Dunlop J. S., Davé R., 2018, *MNRAS*, **480**, 4379

Charlot S., Fall S. M., 2000, *ApJ*, **539**, 718

Chauke P., et al., 2018, *ApJ*, **861**, 13

Chauke P., et al., 2019, *ApJ*, **877**, 48

Chen Y.-P., Trager S. C., Peletier R. F., Lançon A., Vazdekis A., Prugniel P., Silva D. R., Gonçaa A., 2014, *A&A*, **565**, A117

Chen Z., et al., 2020, *ApJ*, **897**, 102

Cheung E., et al., 2012, *ApJ*, **760**, 131

Chevallard J., Charlot S., 2016, *MNRAS*, **462**, 1415

Cid Fernandes R., Mateus A., Sodré L., Stasińska G., Gomes J. M., 2005, *MNRAS*, **358**, 363

Cleveland W. S., Devlin S. J., 1988, *Journal of the American Statistical Association*, **83**, 596

Cole J., et al., 2020, *ApJ*, **890**, L25

Conroy C., 2013, *ARA&A*, **51**, 393

Conroy C., Gunn J. E., 2010, *ApJ*, **712**, 833

Conroy C., Gunn J. E., White M., 2009, *ApJ*, **699**, 486

Cooley J. W., Tukey J. W., 1965, *Mathematics of computation*, **19**, 297

Croton D. J., et al., 2006, *MNRAS*, **365**, 11

Davidson R., Flachaire E., 2008, *Journal of Econometrics*, **146**, 162

Dekel A., Birnboim Y., 2006, *MNRAS*, **368**, 2

Devriendt J. E. G., Guiderdoni B., Sadat R., 1999, *A&A*, **350**, 381

Efron B., 2011, *Journal of Biopharmaceutical Statistics*, **21**, 1052

Efron B., Tibshirani R. J., 1994, An Introduction to the Bootstrap (Monographs on Statistics and Applied Probability). Chapman & Hall/CRC, doi:10.1201/9780429246593

Emsellem E., et al., 2011, *MNRAS*, **414**, 888

Esdaile J., et al., 2021, *ApJ*, **908**, L35

Falcón-Barroso J., Sánchez-Blázquez P., Vazdekis A., Ricciardelli E., Cardiel N., Cenarro A. J., Gorgas J., Peletier R. F., 2011, *A&A*, **532**, A95

Fang J. J., Faber S. M., Koo D. C., Dekel A., 2013, *ApJ*, **776**, 63

Feldmann R., et al., 2006, *MNRAS*, **372**, 565

Forland G. J., Korista K. T., Verner D. A., Ferguson J. W., Kingdon J. B., Verner E. M., 1998, *PASP*, **110**, 761

Forland G. J., et al., 2013, *Rev. Mex. Astron. Astrofis.*, **49**, 137

Feroz F., Hobson M. P., Bridges M., 2009, *MNRAS*, **398**, 1601

Fletcher R., 1987, Practical Methods of Optimization. John Wiley & Sons, Ltd, doi:10.1002/9781118723203

Foreman-Mackey D., Hogg D. W., Lang D., Goodman J., 2013, *PASP*, **125**, 306

Forrest B., et al., 2022, arXiv e-prints, p. arXiv:2208.04329

Franx M., van Dokkum P. G., Schreiber N. M. F., Wuyts S., Labbé I., Toft S., 2008, *ApJ*, **688**, 770

Getreuer P., 2011, *Image Processing On Line*, **1**, 238

Gill P. E., Murray W., Wright M. H., 1981, Practical Optimization. Society for Industrial and Applied Mathematics, doi:10.1137/1.9781611975604

Gill P. E., Murray W., Saunders M. A., 2005, *SIAM Review*, **47**, 99

Golub G. H., 2013, Matrix computations, 4th edition. John Hopkins

Granato G. L., Lacey C. G., Silva L., Bressan A., Baugh C. M., Cole S., Frenk C. S., 2000, *ApJ*, **542**, 710

Greengard L., Lee J.-Y., 2004, *SIAM Review*, **46**, 443

Gustafsson B., Edvardsson B., Eriksson K., Jørgensen U. G., Nordlund Å., Plez B., 2008, *A&A*, **486**, 951

Hamadouche M. L., et al., 2022, *MNRAS*, **512**, 1262

Hansen P. C., 1998, Rank-deficient and discrete ill-posed problems: numerical aspects of linear inversion. Mathematical Modeling and Computation Vol. 4, Siam, Philadelphia, doi:10.1137/1.9780898719697

Hogg D. W., 1999, preprint, (arXiv:astro-ph/9905116)

Huangfu Q., Hall J. A. J., 2017, *Mathematical Programming Computation*, 10, 119

Johnson B., et al., 2021a, dfm/python-fsps: python-fsps v0.4.1rc1, doi:10.5281/ZENODO.4737461

Johnson B. D., Leja J., Conroy C., Speagle J. S., 2021b, *ApJS*, 254, 22

Kabanikhin S. I., 2011, *Inverse and Ill-posed Problems*. de Gruyter, Berlin, doi:10.1515/9783110224016

Kacharov N., Neumayer N., Seth A. C., Cappellari M., McDermid R., Walcher C. J., Böker T., 2018, *MNRAS*, 480, 1973

Kauffmann G., et al., 2003, *MNRAS*, 341, 33

Kriek M., Conroy C., 2013, *ApJ*, 775, L16

Kriek M., van Dokkum P. G., Labbé I., Franx M., Illingworth G. D., Marchesini D., Quadri R. F., 2009, *ApJ*, 700, 221

Lacerda E. A. D., Sánchez S. F., Mejía-Narváez A., Camps-Fariña A., Espinosa-Ponce C., Barrera-Ballesteros J. K., Ibarra-Medel H., Lugo-Aranda A. Z., 2022, *New Astron.*, 97, 101895

Lampinen J., 2002, in Proceedings of the 2002 Congress on Evolutionary Computation. CEC'02 (Cat. No.02TH8600). IEEE, pp 1468–1473, doi:10.1109/cec.2002.1004459

Lawson C. L., Hanson R. J., 1995, Solving least squares problems (SIAM 1995 edition). Classics in applied mathematics Vol. 15, Prentice-Hall Inc., Englewood Cliffs, NJ, doi:10.1137/1.9781611971217

Le Borgne J. F., et al., 2003, *A&A*, 402, 433

Le Fèvre O., et al., 2003, in Jye M., Moorwood A. F. M., eds, Society of Photo-Optical Instrumentation Engineers (SPIE) Conference Series Vol. 4841, Instrument Design and Performance for Optical/Infrared Ground-based Telescopes. pp 1670–1681, doi:10.1117/12.460959

Lena D., et al., 2015, *ApJ*, 806, 84

Levenberg K., 1944, *Quarterly of Applied Mathematics*, 2, 164

Li H., et al., 2018, *MNRAS*, 476, 1765

Lower S., Narayanan D., Leja J., Johnson B. D., Conroy C., Davé R., 2020, *ApJ*, 904, 33

Lower S., Narayanan D., Leja J., Johnson B. D., Conroy C., Davé R., 2022, *ApJ*, 931, 14

MacKay D. J. C., 1992, *Neural Computation*, 4, 415

MacKay D. J. C., 2003, *Information Theory, Inference & Learning Algorithms*. Cambridge University Press, <http://www.inference.org.uk/mackay/itila/>

Maraston C., 2005, *MNRAS*, 362, 799

Maraston C., Strömbäck G., 2011, *MNRAS*, 418, 2785

Maraston C., et al., 2020, *MNRAS*, 496, 2962

Markwardt C. B., 2009, in D. A. Bohlender D. Durand . P. D., ed., *Astronomical Society of the Pacific Conference Series* Vol. 411, *Astronomical Data Analysis Software and Systems XVIII*. p. 251 (arXiv:0902.2850)

Marquardt D. W., 1963, *Journal of the Society for Industrial and Applied Mathematics*, 11, 431

Martin D. C., et al., 2005, *ApJ*, 619, L1

McCracken H. J., et al., 2012, *A&A*, 544, A156

Mendel J. T., et al., 2020, *ApJ*, 899, 87

Mitzkus M., Cappellari M., Walcher C. J., 2017, *MNRAS*, 464, 4789

Moré J. J., 1978, in, *Lecture Notes in Mathematics*. Springer Berlin Heidelberg, pp 105–116, doi:10.1007/bfb0067700

Moré J. J., Garbow B. S., Hillstrom K. E., 1980, User guide for MINPACK-1. Argonne National Laboratory Argonne, IL, <http://cds.cern.ch/record/126569>

Muzzin A., et al., 2013, *ApJ*, 777, 18

Nocedal J., Wright S., 2006, *Numerical Optimization*. Springer Series in Operations Research and Financial Engineering, Springer, New York, doi:10.1007/978-0-387-40065-5

Noll S., et al., 2009, *A&A*, 499, 69

Ocvirk P., Pichon C., Langon A., Thiébaut E., 2006, *MNRAS*, 365, 46

Oh K., Yi S. K., Schawinski K., Koss M., Trakhtenbrot B., Soto K., 2015, *ApJS*, 219, 1

Oh S., et al., 2020, *MNRAS*, 495, 4638

Pozzetti L., Mannucci F., 2000, *MNRAS*, 317, L17

Press W. H., Teukolsky S. A., Vetterling W. T., Flannery B. P., 2007, *Numerical recipes: The art of scientific computing*, 3rd edn. Cambridge Univ. Press, Cambridge, <http://numerical.recipes/book>

Prugniel P., Soubiran C., 2001, *A&A*, 369, 1048

Rubin D. B., 1981, *The Annals of Statistics*, 9

Salim S., Narayanan D., 2020, *ARA&A*, 58, 529

Salpeter E. E., 1955, *ApJ*, 121, 161

Salvato M., Ilbert O., Hoyle B., 2019, *Nature Astronomy*, 3, 212

Sánchez-Blázquez P., et al., 2006, *MNRAS*, 371, 703

Sánchez S. F., et al., 2012, *A&A*, 538, A8

Sánchez S. F., et al., 2016, *Rev. Mex. Astron. Astrofis.*, 52, 21

Sanders D. B., et al., 2007, *ApJS*, 172, 86

Scott N., et al., 2017, *MNRAS*, 472, 2833

Sersic J. L., 1968, *Atlas de galaxias australes*. Obs. Astron. Univ. Nacional de Córdoba, Córdoba

Shen S., Mo H. J., White S. D. M., Blanton M. R., Kauffmann G., Voges W., Brinkmann J., Csabai I., 2003, *MNRAS*, 343, 978

Shetty S., Cappellari M., 2015, *MNRAS*, 454, 1332

Shetty S., Bershady M. A., Westfall K. B., Cappellari M., Drory N., Law D. R., Yan R., Bundy K., 2020, *ApJ*, 901, 101

Silk J., Rees M. J., 1998, *A&A*, 331, L1

Silva L., Granato G. L., Bressan A., Danese L., 1998, *ApJ*, 509, 103

Sobral D., et al., 2022, *ApJ*, 926, 117

Somerville R. S., Davé R., 2015, *ARA&A*, 53, 51

Speagle J. S., 2020, *MNRAS*, 493, 3132

Stanway E. R., Eldridge J. J., 2018, *MNRAS*, 479, 75

Stark P. B., Parker R. L., 1995, *Computational Statistics*, 10, 129

Storey P. J., Hummer D. G., 1995, *MNRAS*, 272, 41

Storn R., Price K., 1997, *Journal of Global Optimization*, 11, 341

Straatman C. M. S., et al., 2018, *ApJS*, 239, 27

Tabor M., Merrifield M., Aragón-Salamanca A., Cappellari M., Bamford S. P., Johnston E., 2017, *MNRAS*, 466, 2024

Tabor M., Merrifield M., Aragón-Salamanca A., Fraser-McKelvie A., Peterken T., Smethurst R., Drory N., Lane R. R., 2019, *MNRAS*, 485, 1546

Tacchella S., et al., 2022, *ApJ*, 926, 134

Taniguchi Y., et al., 2007, *ApJS*, 172, 9

Tojeiro R., Heavens A. F., Jimenez R., Panter B., 2007, *MNRAS*, 381, 1252

Vazdekis A., Sánchez-Blázquez P., Falcón-Barroso J., Cenarro A. J., Beasley M. A., Cardiel N., Gorgas J., Peletier R. F., 2010, *MNRAS*, 404, 1639

Vazdekis A., et al., 2015, *MNRAS*, 449, 1177

Venturi G., et al., 2021, *A&A*, 648, A17

Verro K., et al., 2022a, *A&A*, 660, A34

Verro K., et al., 2022b, *A&A*, 661, A50

Virtanen P., et al., 2020, *Nature Methods*, 17, 261

Voglis C., Lagaris I. E., 2004, in *WSEAS International Conference on Applied Mathematics*. Corfu, Greece

Wake D. A., van Dokkum P. G., Franx M., 2012, *ApJ*, 751, L44

Walcher J., Groves B., Budavári T., Dale D., 2011, *Ap&SS*, 331, 1

Weaver J. R., et al., 2022, *ApJS*, 258, 11

Westera P., Lejeune T., Buser R., Cuisinier F., Bruzual G., 2002, *A&A*, 381, 524

Westfall K. B., et al., 2019, *AJ*, 158, 231

Wilkinson D. M., Maraston C., Goddard D., Thomas D., Parikh T., 2017, *MNRAS*, 472, 4297

Worthey G., 1994, *ApJS*, 95, 107

Worthey G., Faber S. M., Gonzalez J. J., Burstein D., 1994, *ApJS*, 94, 687

Yan R., et al., 2019, *ApJ*, 883, 175

van Dokkum P. G., et al., 2015, *ApJ*, 813, 23

van de Sande J., et al., 2013, *ApJ*, 771, 85

van der Wel A., et al., 2014, *ApJ*, 788, 28

van der Wel A., et al., 2016, *ApJS*, 223, 29

van der Wel A., et al., 2021, *ApJS*, 256, 44

This paper has been typeset from a  $\text{\TeX}$ / $\text{\LaTeX}$  file prepared by the author.